POLITECNICO DI MILANO

Facoltà di Ingegneria dei Sistemi
Corso di Laurea specialistica in Ingegneria Fisica
Orientamento Nanotecnologie

Dipartimento di Fisica

STRUCTURAL AND ELECTRICAL CHARACTERIZATION OF GRAPHENE AFTER ION IRRADIATION

Tesi di Laurea di:
Valentina DI CRISTO
Matr. n. 733682

Relatore: Prof. **Lamberto DUÒ**

Anno Accademico 2009-2010

22 Ottobre 2010

Aknowledgments

My first thanks are to Pr. Klaus Leifer, who gave me the opportunity to work in his group and to discover the world of research, which excited me right away. Thanks to all ElMiN group: Stefano, Tobias, Hassan, Timo and Sultan. Thanks to Göran, who allowed us to work in his lab and to accomplish this work. Thanks to Matt for the essential support with the Raman measurements and for some good talks.
Thanks to the patience that Tobias and Hassan have had day-by-day in teaching me my job and in answering all my questions. Thanks to Tobias to have taught me that some people are able to eat pasta with ketchup! Thanks to Stefano for his support and his innumerable advices, both personal and professional, that he gave me in all the time spent working with him; thanks for the devoted job he did to help me in the writing of my thesis. Everything he taught me is of great value.
A big thanks to my Pr. Lamberto Duo', I could say the official adviser during all my academic experience. His support, experience and advices are, and always will be, of a immense value for me.

Thanks to all the fantastic people I met in this wonderful experience in Uppsala.
Thanks to Emma, Lucy and Ben, who became my family during this year spent far from home. Their company, support and love was of an inestimable value for me. They allowed me to live this amazing experience with serenity and happiness, sharing with me the good moments, as well as the more difficult ones.
Thanks to Filo, for his advices and recommendations that helped me to face this experience in the best way.

Con profonda gratitudine ringrazio mamma e papà che mi hanno sostenuto nel miglior modo possibile, con tanti sacrifici e tanto amore durante tutta la mia vita e tutta la durata dei miei studi. E' grazie a loro se sono arrivata con successo a questo traguardo importante della mia vita.
Un pensiero speciale anche ai miei nonni, che hanno sempre creduto in me e il cui supporto ha avuto un ruolo fondamentale per il sereno compimento dei miei studi.

Abstract

Graphene is a recently discovered material consisting of a two-dimensional sheet of Carbon atoms arranged in an hexagonal pattern. It is a zero-gap semimetal whose electrical properties can be tuned by controlled induction of defects such as vacancies. In this work, graphene flakes were produced with the standard method of mechanical exfoliation. Afterward, we have used light optical microscopy (LOM), atomic force microscopy (AFM), Raman spectroscopy and in-situ electrical measurements to investigate the changes in structural and electrical properties after defect introduction by ion irradiation. The ion bombardment was performed with two different systems, a focused ion beam at the Microstructure laboratory and an ion accelerator at the Tandem laboratory, both at Uppsala University. The main goal of the work was to develop and test a contacting scheme for the graphene flakes that would allow us to perform in-situ I-V measurements during defect insertion. In this respect, the project was a success. The different characterization techniques yielded different types of information. LOM is useful as a first screening to identify the graphene candidates; Raman spectroscopy can provide information on both the flake thickness (mono-layer or multi-layer) and on the defect density, although the latter only qualitatively. The AFM analysis did not give significant results as it could not unambiguously discern any sign of ion impact neither on the graphene flakes nor on the substrate.

Sintesi

Questo lavoro di tesi è stato svolto presso il Dipartimento di 'Microscopie Elettroniche e Nanotecnologie' dell'università di Uppsala, Svezia.
Il lavoro consiste nello studio sia delle proprietà strutturali che elettriche del grafene prima e dopo induzione di difetti.

Il grafene è una cristallo bidimensionale prodotto per la prima volta nel 2004 da un gruppo di ricercatori dell'università di Manchester; grazie alla sue straordinarie proprietà elettroniche è diventato uno dei materiali più studiati degli ultimi anni. Consiste di un singolo strato atomico di atomi di carbonio ibridizzati sp^2 arrangiati in una struttura esagonale. La forza dei legami sp^2 degli atomi di carbonio rispetto ai legami Van der Waals che tengono insieme i vari strati di grafene fino a formare grafite, permette di isolare singoli strati atomici con una bassa densità di difetti reticolari.

L'interesse nello studio del grafene difettato deriva dal fatto che la presenza di difetti può cambiare drasticamente sia le sue proprietà termiche che quelle elettroniche. Studi teorici e sperimentali hanno mostrato un significativo aumento della conducibilità dopo l'inserimento di un certo numero di difetti. Questo fatto può essere attribuito alla formazione di livelli energetici intermedi che crea una regione intorno al difetto che esibisce un comportamento metallico. Inoltre, difetti reticolari introducono centri di scattering, che possono trasformare il grafene da conduttore a isolante. La dipendenza della conduttività del grafene dalla concentrazione di difetti è di cruciale importanza per la formazione di giunzioni elettroniche nei dispositivi elettronici (par. 3.2). La difettosità è dovuta per la maggior parte al processo di produzione, ma anche dall'interazione del grafene con il substrato o l'ambiente esterno. Tuttavia un significativo numero di difetti può essere introdotto intenzionalmente, per esempio attraverso bombardamento ionico, con lo scopo di modificare e progettare le proprietà del grafene.

La tecnica utilizzata in questo lavoro per la produzione dei fiocchi di grafene viene chiamata *esfoliazione meccanica,* in cui un campione di grafite artificiale ad alta qualità

cristallina viene esfoliata tramite l'uso di nastro adesivo. Il nastro adesivo viene fatto aderire sulla superficie di uno dei lati del cubo di grafite. Quando il nastro viene rimosso, un sottile strato di materiale rimane attaccato sulla superficie del nastro stesso. I residui di grafite vengono poi successivamente affinati ripiegando ripetutamente il nastro adesivo su se stesso fino a che dei fiocchi abbastanza sottili sono stati prodotti (par. 4.1).
Il risultato dell'esfoliazione viene trasferito su un substrato di silicio ricoperto da 300 nm di biossido di silicio a fine di poter procedere con l'identificazione e la caratterizzazione dei fiocchi di grafene tramite l'uso di *Microscopio Ottico* (par. 4.2.1), *Microscopio a Forza Atomica* (par. 4.2.2), e *Spettroscopia Raman* (par. 4.2.3).

Il processo di esfoliazione produce grani e fiocchi di svariate dimensioni e spessore. Ovviamente non tutti sono utili nello studio del grafene, ma solo quei fiocchi che abbiano uno spessore non maggiore di qualche strato atomico.
Il microscopio ottico viene utilizzato in prima analisi per l'identificazione di buoni candidati. Questo è permesso dal fatto che un accurata scelta dello spessore dello strato di biossido di silicio garantisce un contrasto sufficiente perché anche fiocchi di ridotte dimensioni e spessore fino a pochi ångström possano essere visualizzate al microscopio ottico.
Una volta che candidati promettenti sono stati identificati è opportuno analizzare i fiocchi tramite il microscopio a forza atomica. Questo permette di ottenere un immagine topografica della superficie del fiocco e ottenere una stima dello spessore.
La spettroscopia Raman, grazie alle differenze dello spettro caratteristico di un singolo strato atomico rispetto a un doppio o multi strato, permette in ultima analisi una valutazione dello spessore del fiocco.

Contatti elettrici sul fiocco vengono depositati tramite litografia a fascio elettronico (par. 4.3) per permetterne la caratterizzazione elettrica.

I difetti sono stati introdotti in maniera controllata tramite bombardamento ionico in tre diversi esperimenti (cap. 5).
Nel primo esperimento un fiocco di grafene contattato elettricamente è stato irradiato per mezzo di un acceleratore ionico con ioni di Carbonio 3+ a 12 MeV. L'obiettivo di

questo primo esperimento era quello di testare il dispositivo costruito e la fattibilità di misure elettriche *in situ*.
Nel secondo esperimento quattro diversi campioni sono stati irradiati in due diversi modi: un fiocco contattato elettricamente è stato bombardato con protoni a 2 MeV, mentre tre fiocchi non contattati sono stati bombardato con ioni di Iodio 7+ a 40 MeV.
Nel terzo esperimento un fiocco elettricamente contattato è stato irradiato tramite un *Fascio Ionico Focalizzato* con ioni Gallio accelerati a 30 kV.
Tutti i campioni sono stati caratterizzati tramite microscopio a forza atomica e spettroscopia Raman prima e dopo il bombardamento ionico. I campioni contattati sono stati inoltre caratterizzati elettricamente durante il bombardamento.

Dai risultati ottenuti possiamo concludere che il microscopio a forza atomica non è lo strumento ottimale per analizzare gli effetti del bombardamento ionico e i difetti sul grafene. La spettroscopia Raman fornisce informazioni utili riguardo ai cambiamenti della struttura del grafene dovuti alla variazione della densità dei difetti. Tuttavia le informazioni ottenute sono di carattere qualitativo e non sono in grado di fornire informazioni quantitative circa il numero di difetti e la loro struttura.

Il risultato di maggior importanza ottenuto in questo lavoro per questa fase dell'esperimento, è senza dubbio la realizzazione di un dispositivo funzionante in grado di misurare le variazioni della conducibilità del fiocco di grafene durante il bombardamento ionico sia per mezzo dell'acceleratore ionico che per mezzo del fascio ionico focalizzato.

Contents

1. Introduction

This work is focused on the production, the characterization and the analysis of defected graphene.

Carbon-based materials, such as diamond, graphite, carbon nanotube, and graphene have been of great interest in various fields of nanotechnology. So far, many applications of the carbon-based materials have been demonstrated, such as field effect transistors, chemical and bio sensors, nanocomposites, and quantum devices. Among those materials, graphene, a two dimensional zero-gap semiconductor consisting of a single layer of carbon atoms arranged in a hexagonal pattern, has received a large interest since the first report on the electric field effect. Graphene has been shown to possess several interesting electronic properties such as the transport of relativistic Dirac fermions, bipolar supercurrents, spin transport, and quantum Hall effect at room temperature. Graphene also attracted considerable interest in the application to ambipolar field effect transistors, gate controlled p-n junctions, ultrasensitive gas sensors, and nanoribbons. Moreover, recent studies have suggested that graphene can serve as a building block for carbon-based integrated nanoelectronics [1].

The strong carbon-carbon sp^2 bonds which provide graphene with high intrinsic strength and make possible the isolation of single atomic layers, also result in a very low density of lattice defects in graphene prepared by mechanical exfoliation. However, lattice defects in graphene are of great theoretical interest as a source of intervalley scattering which in principle transforms graphene from a metal to an insulator. Hence, understanding their impact on electronic transport is important [2].

Defects predominantly occur during the production process, while another unavoidable source of additional disorder is the interaction with the substrate and environment. However, defects can also be introduced intentionally, e.g. by ion bombardment, in order to engineer the properties of graphene [3].

Several theoretical works pointed out that defects in graphene bring substantial changes in the electronic states near the Fermi level: these states are of great importance since many of the unique properties of graphene originate from the topology of its electronic

bands in the vicinity of the Dirac point. Consequently, it is of particular importance to have a thorough understanding of the physics of defects and disorder in graphene [3].

In this work, mono and bilayer graphene flakes were exfoliated on Si wafers topped by a 300 nm thick SiO_2 surface layer. The flakes were then irradiated with the aim of inducing defects in the material in a controlled way. To try to achieve this, ion irradiation experiments were carried out in the Tandem laboratory of Uppsala University. The atomic species used were 40 MeV Iodine ions (I^{7+}) and 2 MeV protons (H^{+}). Another irradiation experiment was performed using 30 keV Ga ions with the focused ion beam (FIB) at the Ångström laboratory.

Atomic force microscopy (AFM) and Raman spectroscopy were used to characterize the change in the graphene structure and the mechanism of disorder formation in single layer and bilayer graphene. Electrical measurements before, during and after irradiation were also carried out.

Raman spectroscopy is a useful tool to have information about the flake thickness and also provides some useful information about the change in the structure of the graphene flake due to the change in defect density. However, the information obtained by Raman spectroscopy is qualitative, and cannot provide any quantitative information about the amount of defects nor their structure. AFM analysis, on the other hand, did not give any significant result making the AFM not the optimum tool to study defects on graphene and investigate the effects of ion irradiation.

The most important achievement of this work at this stage of the experiment is, doubtless, the realization of a working setup able to measure in situ the change of the conductivity of the graphene flake under ion irradiation both in the Tandem ion accelerator and in the FIB.

2. Theory

2.1 Graphene theory

Graphite is the most allotropic form of carbon. It consists of parallel sheets of sp^2 hybridised carbon atoms tightly packed into a two-dimensional honeycomb lattice. The sheets are 0.335 nm apart and held together by the weak bonding of the remaining non-hybridised p electrons. The C atoms in every sheet form hexagons with sides 0.142 nm long (Fig. 2.1). Graphite has been known to mankind since prehistoric times and has nowadays many applications that range from dry lubricant, neutron moderator, crucibles and pencils (where its greek name comes from).

Since the p-bonding between the sheets is much weaker than the sp^2-bonding within a sheet, single layers can be extracted from a graphite crystal with appropriate methods.

Graphene is the name given to such an isolated monolayer of graphite. It can be considered the basic building block for graphitic materials of all other dimensionalities [4].

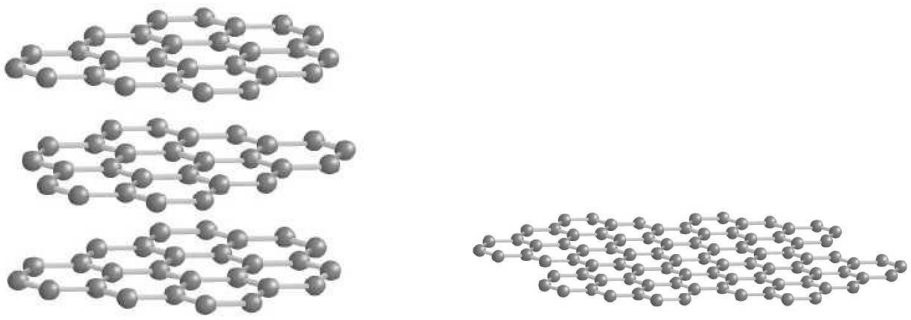

Fig. 2.1 Graphene to graphite relation (left). Crystallographic structure of graphene (right).

More than 70 years ago, it was proved that 2D crystals would be thermodynamically unstable and therefore could not exist [5]. In 2004 Geim and Novoselov performed an experiment at the University of Manchester, showing that it was possible to isolate "free state" graphene flakes. The apparent incongruity stems from the fact that, even though

graphene is monoatomically thin (and could thus be considered two-dimentional), it can become thermodynamically stable by either interacting with a supporting substrate or, in case of free-standing graphene, by forming a corrugated surface [6].
As a result of its extraordinary electronic properties, graphene has become one of the most studied materials of the recent years.

2.1.1 Zero-gap semiconductor

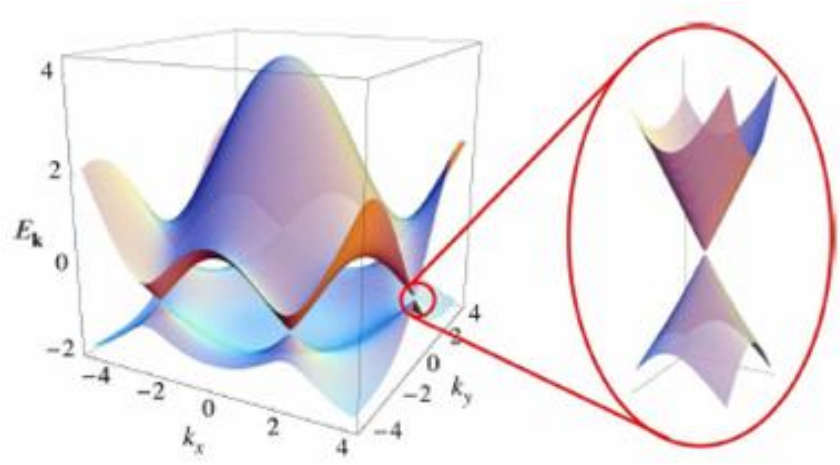

Fig. 2.2 Zero-gap energy spectrum of graphene.

Graphene is a two-dimensional zero-gap semiconductor (Fig. 2.2) with its charge carriers formally described by the Dirac-like Hamiltonian:

$\hat{H}_0 = -iv_F\hbar\sigma\Delta$

where $v_{F \approx 10^6}$ ms^{-1} is the Fermi velocity, and $\sigma = (\sigma_x,\sigma_y)$ are the Pauli matrices [7].
The fact that charge carriers in graphene are described by the Dirac-like equation rather than the usual Schrödinger equation can be seen as a consequence of graphene's crystal structure, which consists of two carbon sublattices A and B (Fig. 2.3).

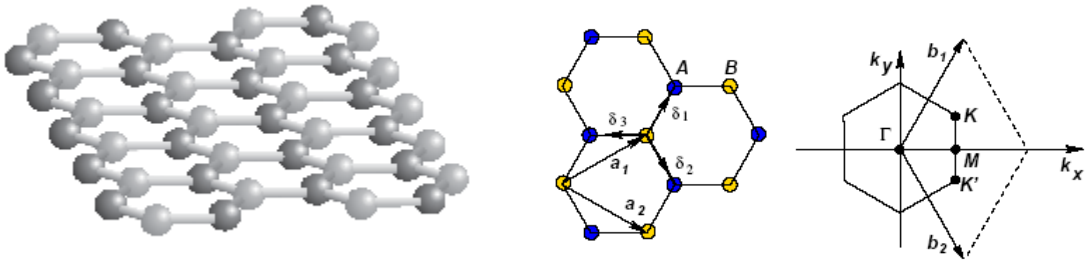

Fig. 2.3 Lattice structure of graphene, made out of two interpenetrating triangular lattices (a_1 and a_2 are the lattice unit vectors, and δ_i, I = 1, 2, 3 are the nearest neighbour vectors). On the right the corresponding Brillouin zone.

Quantum mechanical hopping between the sublattices leads to the formation of two energy bands, and their intersection near the edges of the Brillouin zone yields the conical energy spectrum near the Dirac points K and K' (Fig. 2.4). As a result, quasiparticles in graphene exhibit the linear dispersion relation $E = \hbar k v_F$, as if they were massless relativistic particles [7].

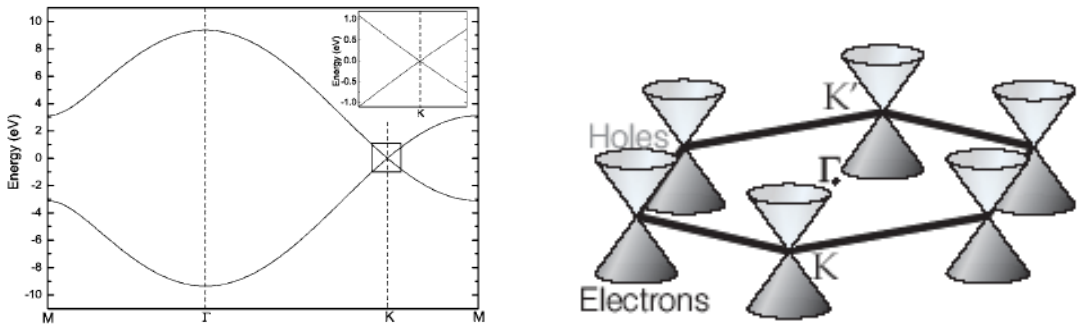

Fig. 2.4 Band structure of grapheme (left). The conductance band touches the valence band at the K and K' points (right).

Electrons and holes in condensed matter physics are usually described by different equations, however, electron and hole states in graphene are interconnected. Graphene´s quasiparticles have to be described by two-component wavefunctions, which are needed to define the relative contributions from sublattices A and B [7].

By analogy with QED (Quantum Electrodynamics), one can also introduce a quantity called *chirality* that is formally a projection of σ on the direction of motion k and is positive for electrons and negative for holes. In essence, *chirality* in graphene signifies the fact that K electron and $-K$ hole states are intimately connected because they

originate from the same carbon sublattice. Many electronic processes in graphene can be understood as due to conservation of *chirality* [4].

2.1.2 Klein paradox

One consequence of the *chiral* nature of graphene is the anomalous behaviour concerning electron tunnelling through potential barriers. This is known as Klein paradox (Fig. 2.5). The notion of Klein paradox refers to a counterintuitive process of perfect tunnelling of relativistic electrons through arbitrarily high and wide barriers [4]. In other words, an incoming electron starts penetrating through a potential barrier if its height V_0 exceeds twice the electron's rest energy mc^2 (m is the electron mass, c is the speed of light). In this case, the transmission probability T depends only weakly on the barrier height, approaching the perfect transparency for very high barriers. This is in stark contrast with the conventional, nonrelativistic tunnelling where T exponentially decays with increasing V_0. This relativistic effect can be attributed to the fact that a sufficiently strong potential, being repulsive for electrons, is attractive for holes and results in positron states inside the barrier, matching between electron and hole wavefunctions across the barrier leads to the high-probability tunnelling described by the Klein paradox [7].

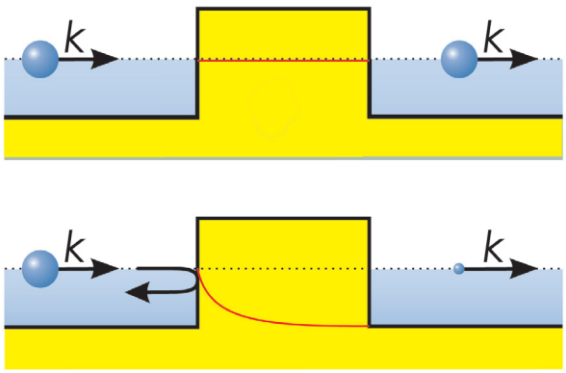

Fig. 2.5 Tunnelling in condensed matter: Tunnelling of grapheme (top), conventional semiconductor (bottom).

Experimental results have shown that the barrier remains perfectly transparent for angles close to the normal incidence $\Phi = 0$. This is a feature unique to massless Dirac fermions and directly related to the Klein paradox in QED [7].

2.1.3 Quantum Hall effect

The most striking demonstration of the massless character of the charge carriers in graphene is the anomalous quantum Hall effect (QHE). In a two-dimensional system with a constant magnetic field **B** perpendicular to the system plane the energy spectrum is discrete (Landau quantization). In the case of massless Dirac fermions the energy spectrum takes the form

$$E_{v\sigma} = [2 \left| e \right| \boldsymbol{B}\hbar \mathbf{v}_F^2 \, (v + ½ \pm ½)]^{½}$$

where $\mathbf{v}_F$ is the electron velocity, $v = 0, 1, 2, \ldots$ is the quantum number and the term with $\pm ½$ is connected to the *chirality* [7].

An important peculiarity of Landau levels for massless Dirac fermions is the existence of zero-energy states (with $v = 0$ and minus sign in the equation above). This situation differs fundamentally from usual semiconductors with parabolic bands dispersion where the first Landau level is shifted by $\hbar\omega_c$ / 2. The existence of the zero-energy Landau level leads to an anomalous QHE with *half-integer* quantization of the Hall conductivity, instead of the *integer* one (Fig. 2.6). Usually, all Landau levels have the same degeneracy which is just proportional to the magnetic flux through the system. For the case of massless Dirac electrons, the zero-energy Landau level has degeneracy two times smaller than any other level [7].

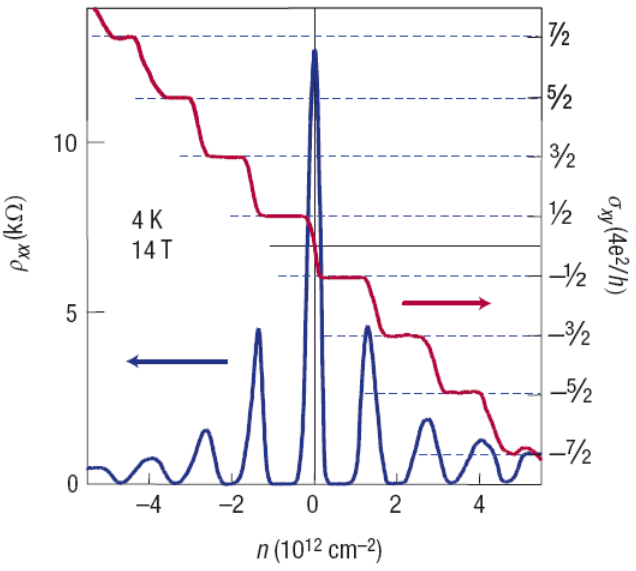

Fig. 2.6 Chiral quantum Hall effect. The hallmark of massless Dirac fermions is QHE plateau in σ_{xy} at halfintegers of $4e^2/h$

2.1.4 Finite minimal conductivity

A remarkable property of graphene is its finite minimal conductivity which is of the order of the conductance quantum e^2/h.
This is the "quantization" of conductivity rather than conductance. This phenomenon is intimately related with the quantum-relativistic phenomenon known as *Zitterbewegung* (trembling-motion), which is connected to the uncertainty of the position of relativistic quantum particles due to the inevitable creation of particle-antiparticle pairs at the position measurements [7].
Another approach to a qualitative understanding of the minimal conductivity is based on the Klein paradox. In a conventional two-dimensional system, strong enough disorder results in electronic states that are separated by barriers with exponentially small transparency. In contrast, in graphene, all potential barriers are relatively transparent. This does not allow charge carriers to be confined by potential barriers that are smooth on an atomic scale. Therefore, different electron and holes "puddles" induced by disorder are not isolated but they effectively percolate, thereby suppressing localization. In the absence of localization, the minimal conductivity (e^2/h) can be obtained by assuming that the mean-free path cannot be smaller than the electron wavelength [7].

2.2 Characterization

2.2.1 Detection and light optical microscopy

A non trivial aspect regarding the production of graphene is its identification. This is due to the fact that a graphene sheet, being atomically thin, is really difficult to be observed under an optical microscope. In fact graphene can only be seen when deposited onto an appropriated bilayered substrate with a finely tuned thickness of the topmost layer.
The obtained graphene can be detected by the use of a light optical microscope (LOM) thanks to the difference in the optical path of light made by the layer on top of the substrate [8].
It is found that graphene becomes visible in the LOM if placed onto a silicon wafer with a 300 nm thick SiO_2 layer on top of it.

The theory of quantifying the contrast takes into account the refractive index of Si, SiO_2 and graphene and the relative intensity of reflected light in presence and absence of graphene [8].

It has to be noted, however, that the theory slightly but systematically overestimates the contrast. Fig. 2.7 shows a colour plot for the expected contrast as a function of SiO_2 thickness and illuminating wavelength. This plot can be used to select the most appropriate filter for a given thickness of SiO_2. By using filters, graphene can be visualized on top of SiO_2 of practically any thickness (except for ≈150 nm and below 30 nm) [9].

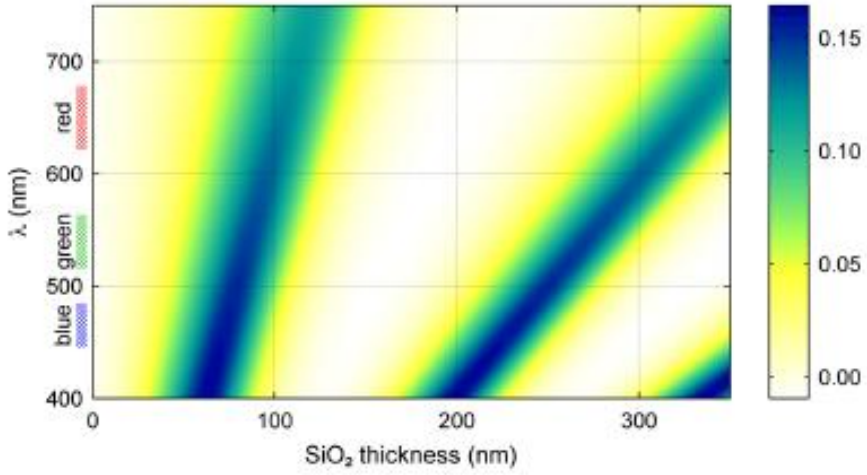

Fig. 2.7 Colour plot of the contrast as a function of illumination wavelength and SiO_2 thickness [9].

Note, however, that the use of green light is most comfortable for eyes that, in our experience, become rapidly tired when using high-intensity red or blue illumination. This makes SiO_2 thicknesses of approximately 90 nm and 280 nm most appropriate with the use of green filters as well as without any filter, in white light. In fact, the lower thickness of 90 nm provides a better choice for graphene's detection, and it might be a good substitute for the present benchmark thickness of 300 nm. Furthermore, the changes in the light intensity due to graphene are relatively minor, and this allows the observed contrast to be used for measuring the number of grapheme layers [9].

The importance of this step will become clear when the method for producing graphene is taken into consideration. Mechanical exfoliation from bulk graphite produces a great number of flakes on the silicon wafer, but only a few of them are mono- or bilayers. It is essential therefore to have a fast method, such as LOM, for identifying possible candidates for graphene among all the flakes produced.

2.2.2 Atomic force microscopy

Once possible graphene candidates have been screened by LOM, their actual thickness can be estimated by use of the Atomic Force Microscope (AFM).

The Atomic Force Microscope, which has been invented in 1986, is nowadays one of the most spread techniques for nanoscale investigation on surfaces. It can work both on hard and soft samples, either in air, vacuum or liquids and it can achieve atomic resolution under particular conditions and setting. It measures the interaction forces acting between a fine tip and a sample. The tip is attached to the free end of a cantilever and is brought very close to the surface. Attractive or repulsive forces resulting from interactions between the tip and the surface will cause a positive or negative bending of the cantilever. This results in different operation modes which should be chosen according to the characteristics of the sample, since each mode has different advantages and disadvantages.

The bending is detected by use of a laser beam, which is reflected from the back side of the cantilever and collected in a photodiode. An active feedback loop adjusts tip-sample distance by means of a piezoelectric actuator in order to maintain the interaction constant. During the acquisition, a computer saves the feedback signal as a function of position while the tip is scanned over the sample. Fig. 2.8 shows a sketch of the system.

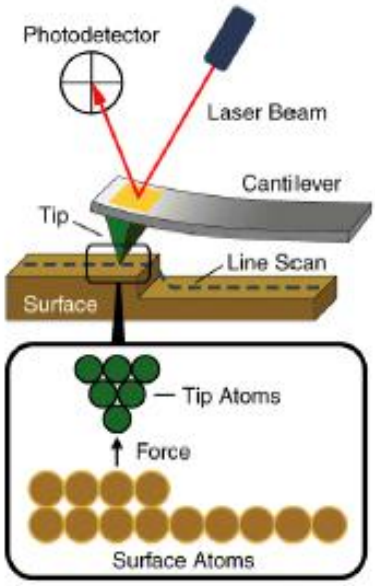

Fig. 2.8 Block diagram of AFM.

A force sensor in the AFM can only work if the probe interacts with the force field associated with a surface. The dependence of the van der Waals force upon the distance between the tip and the sample is shown in Fig. 2.9.

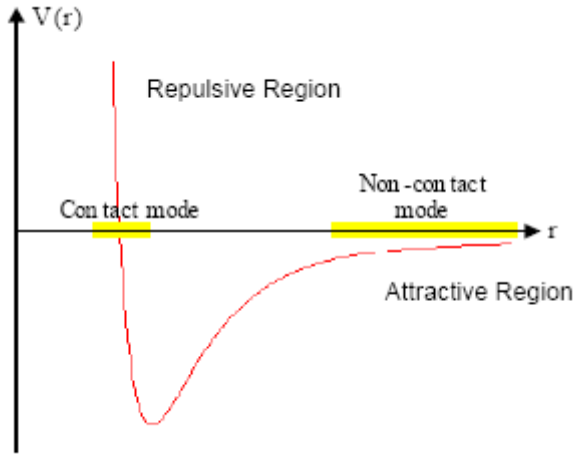

Fig. 2.9 Dependence of the potential energy vs the distance between tip and sample during their reciprocal interaction.

The operation modes of AFM can be distinguished according to the cantilever dynamics and the relevant tip-sample interactions. Depending on whether the cantilever is oscillating or not, the AFM operation can be *static* if the cantilever does not vibrate during imaging, or *dynamic* if the cantilever is exited to vibrate at or off its resonance frequency.

In static mode, also called *contact mode*, the tip is brought in contact with the sample and the AFM works with the tip in repulsive contact with the surface. This can be achieved via scanning in constant force mode or in constant height mode. Constant force mode is based upon the static measurements of deflection of the cantilever. Topographic images are recorded by scanning the tip over the sample surface at a constant cantilever deflection. The tip is brought into the repulsive force regime and the position of the tip is given by an equilibrium of forces. In constant height mode the distance between tip and sample is kept constant. The feedback circuit is turned off and the deflection of the cantilever is directly used for the height signal in the topography map.

In *dynamic mode* the tip does not touch the surface and the probe operates in the attractive force region. The use of non-contact mode allows scanning without influencing the shape of the sample by the tip-sample interaction.

The cantilever is made externally to oscillate nearly or exactly close to its resonance frequency $f_{res} = 1/2\pi\ (k/m)^{½}$ where m is the cantilever mass and k its elastic constant. Forces that act between the sample and the tip will not only cause a change in the oscillation amplitude, but also change in the resonant frequency and phase of the cantilever. The amplitude is used for the feedback and the vertical adjustment of the piezoscanner is recorded as a height image. Simultaneously, the phase changes are presented in the phase image [10].

An AFM cantilever should have a high resonant frequency to boost the sensitivity, thus evidently its mass needs to be very small (k is low already because of the low stiffness requirement). When the tip approaches the surface, its resonance frequency decreases due to van der Waals and long-range forces. A servo adjusts the tip-to-sample distance accordingly to maintain either frequency or amplitude constant. The system acquires the local topography from the change in the resonant frequency and the signal from the feedback loop at every point (x,y) of the surface. In amplitude modulation mode the cantilever oscillator is driven at a constant frequency. A change is the force's derivate results in a shift in the amplitude of the cantilever vibration and the feedback signal is derived by measuring the amplitude change. Once the working condition set by the feedback set-point are reached, the driving circuit controls the tip-sample distance through the piezoelectric system in order to maintain a constant oscillation amplitude. In this way a map of the sample at constant force gradient is acquired during the scanning process. Moreover, amplitude modulation allows distinguishing the different materials on a surface from phase changes in the oscillation.

In *frequency modulation* mode the signal used to produce the image comes from the direct measurements of the resonance frequency of the cantilever, which is modified by the tip-surface interaction. The cantilever is kept oscillating at its current resonance frequency with a constant amplitude. The driving signal of the cantilever oscillation is generated through a feedback loop where the a.c. signal coming from the cantilever motion detector is used as excitation signal. The spatial dependence of the frequency shift induced in the cantilever motion by the tip-sample interaction is used as source of contrast. During the scan the tip-sample distance is varied in order to achieve a set value for frequency shifts, thus the topography represents a map of constant frequency shift over the surface. The use of high stiffness cantilevers, in this case, yields high stability near the surface and true atomic resolution in ultra-high vacuum.

Non-contact mode is non-invasive and has much less risk of sample or tip damage, but can be affected by some unwanted edge effects that reduce its sensibility when performed in air [11].

This imaging technique has many big advantages: it yields a truly 3D scanning of the surface, recording 3 coordinate values (x,y,z) for each point of the surface scanned with picometric precision and the samples can be of any electrical kind, insulating or conductive, as compared to other scanning probe microscopes, such as scanning tunnelling microscope (STM), that require samples with good conductivity. On the other hand AFM presents some drawbacks: the image size is limited to tens or hundreds of micrometers as well as the maximum measurable height which is some microns too (hence the depth of field is limited); the tip shape and condition can produce image aberrations or artefacts. AFM tips are in fact rounded off with a radius of curvature of some nanometers, although the tip can be differently shaped according to the necessity. The tip must have a high aspect ratio to probe accurately features like steep edges, pits and crevices, thus it should be as long and thin as possible. If it is too wide and/or short, it might start sensing some step edges before the actual tip apex passes over them, resulting in blurred or rounded imaged edges [12].
The final image and its resolution will be a non linear function of the distance dependence of the interaction, the tip radius and the microscope sensitivity.
The vertical resolution in AFM in virtually zero and is limited only by the sensitivity (signal-to-noise ratio) and most commercial AFM can today reach a vertical resolution of 0.01 nm. The lateral resolution depends on the tip radius, on the topography and defects shape and on their relative height. The good condition of the tip is also crucial to obtain the best resolution. In contact-mode the interaction force is too big to obtain truly atomic resolution, whereas in non contact mode the resolution can be limited by the size of the tip-sample gap. True atomic resolution can be achieved with frequency modulation mode in UHV where the interaction forces are very low.

In the case of graphene, though, due to the chemical contrast between graphene and the substrate (which results in an apparent chemical thickness of 0.5-1 nm, much bigger than what can be expected from the interlayer graphite spacing), in practice, it is only possible to distinguish between one and two layers by AFM if films contain folds or wrinkles [13]. See paragraph 4.2.2.

2.2.3 Raman spectroscopy

A further analysis step in the detection and analysis of single layer graphene is Raman spectroscopy. Raman fingerprints for single layers, bilayers, and few layers reflect changes in the electron bands and allow unambiguous, high-throughput, nondesctructive identification of graphene layers [13], other than the analysis of defects in the graphene sheet.

Raman spectroscopy is a spectroscopic technique based on inelastic scattering of monochromatic light, usually from a laser source (Fig. 2.10.a). Inelastic scattering means that the frequency of photons in monochromatic light changes upon interaction with a sample. Photons of the laser light are absorbed by the sample and then reemitted. The frequency of part of the reemitted photons is shifted up or down with respect to the original monochromatic frequency, which is called the Raman effect. This shift provides information about vibrational, rotational and other low frequency transitions in molecules.

The Raman effect is based on molecular deformations in an electric field E determined by the molecular polarizability α. The laser beam can be considered as an oscillating electromagnetic wave with electrical vector E. Upon interaction with the sample it induces an electric dipole moment P = αE which deforms molecules. Because of periodical deformation, molecules start vibrating with a characteristic frequency υ_m.
In other words, monochromatic laser light with frequency υ_0 excites molecules and transforms them into oscillating dipoles. Such oscillating dipoles emit light of three different frequencies when: 1) a molecule with no Raman-active modes absorbs a photon with the frequency υ_0, the excited molecule returns back to the same basic vibrational state and emits light with the same frequency υ_0 as an excitation source. This type of interaction is called an elastic *Rayleigh scattering*; 2) a photon with frequency υ_0 is absorbed by a Raman-active molecule in its basic vibrational state. Part of the photon's energy is transferred to the Raman-active mode with frequency υ_m and the resulting frequency of scattered light is reduced to υ_0 - υ_m. This Raman frequency is called Stokes frequency, or just *Stokes*; 3) a photon with frequency υ_0 is absorbed by a Raman-active molecule, which, at the time of interaction, is already in an excited vibrational state. Part of the energy of the excited Raman-active mode is released, the

molecule goes to a lower vibrational state and the resulting frequency of scattered light goes up to $\upsilon_0 + \upsilon_m$. This Raman frequency is called Anti-Stokes frequency, or just *Anti-Stokes*. A sketch of the Raman effect is shown in Fig. 2.10.b [14].

A typical Raman spectrum (Fig. 2.10.c) will then show the measured shift in the frequency of the reemitted light with respect to the exciting radiation and will have a strong peak around 0 cm^{-1} (unless a filter is used to block this signal).

The stokes and anti-stokes band will appear at symmetric positions of either side of 0. Normally stokes bands are stronger than anti-stokes, depending on the sample temperature and on the energy spacing of the vibrational levels (anti-stokes band should not appear at 0 K).

a)

b)

c)

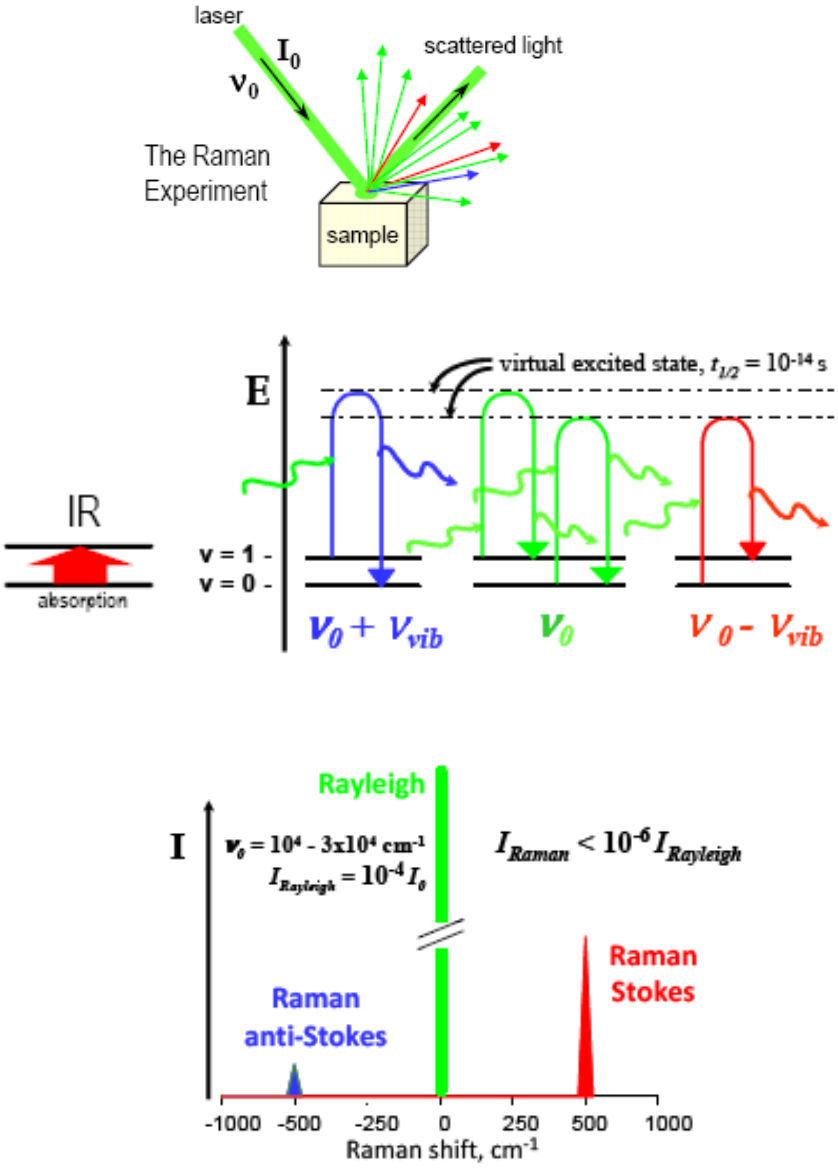

Fig. 2.10 Raman spectroscopy: a) laser-sample interaction; b) Raman effect; c) Raman spectrum

About 99.999% of all incident photons in spontaneous Raman undergo elastic Rayleigh scattering. This type of signal is useless for practical purposes of molecular characterization. Only about 10^{-4} % of the incident light produces inelastic Raman signal with frequencies $\upsilon_0 \pm \upsilon_m$ [14].

Raman spectroscopy is a very important analysis technique in the field of carbon research and has historically played an important role in the structural characterization of graphitic materials [15]. In fact, this spectroscopy technique allows to distinguish clearly between single and multilayer graphene thanks to the fact that Graphene vibrational properties depend on thickness of the flakes and this is reflected in the characteristic spectral features [16]. Fig. 2.11 shows a Raman spectrum of monolayer graphene with respect to the Raman spectrum of graphite.

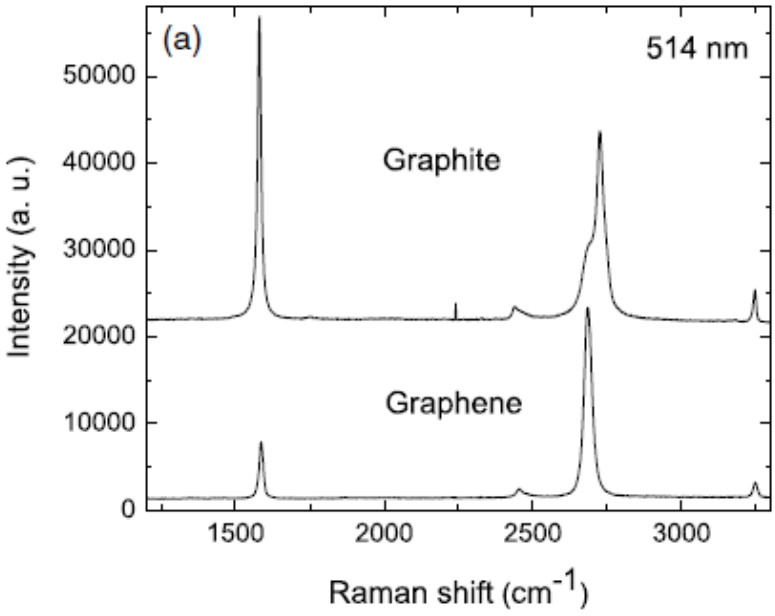

Fig. 2.11 Raman spectra of graphite (top) and graphene (bottom) [13].

Graphene has two fundamental hallmarks: a first peak at around 1580 cm^{-1} named the G peak, and a second band around 2700 cm^{-1} called the G' or 2D peak. The shape of the 2D peak, in monolayer graphene, is sharp, narrow and centered at 2700 cm^{-1}. This peak broadens in thicker flakes, as already in bilayers is the resulting envelop of four sub-peaks (Fig. 2.12) [15]. The position of the G peak shifts towards lower frequencies and its intensity increases significantly as the thickness grows. In graphene the G peak is

smaller than the 2D while, already for bilayers and thicker flakes, the G peak is prominent.

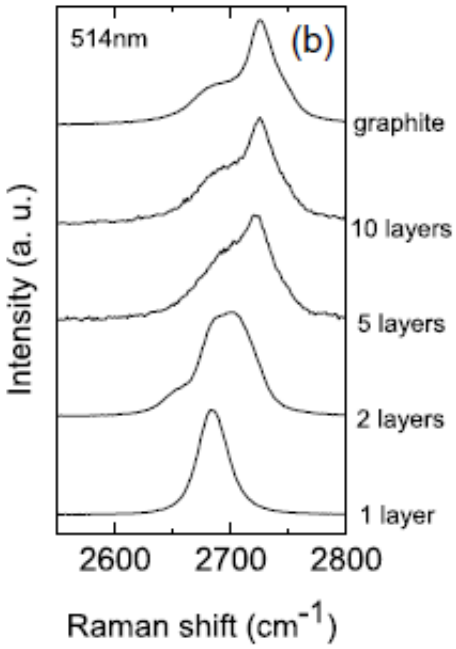

Fig. 2.12 Evolution of the 2D peak from monolayer graphene to bulk graphite. The 2D peak's shape changes with respect to the thickness of the sample [13].

2.3 Electron beam lithography

In order to carry out the electrical characterization of the graphene flakes, every flake has to be electrically contacted and connected to a high precision multimeter. The contacting process is based on the use of electron beam lithography (EBL), a lithographic process that uses a focused beam of electrons to form a pattern onto a wafer. EBL offers higher patterning resolution than optical lithography because of the shorter wavelength of the 10-50 keV electrons (0.2-0.5 Å) that it employs.

As in optical lithography, there are two types of e-beam resists: positive tone and negative tone: positive resists on exposed regions will be removed during development, whereas in the case of negative resist the exposed region remains after development. The most common resists are polymers dissolved in a liquid solvent. The compound is dropped onto the substrate, which is then spun at 1000 to 6000 rpm to

form a coating. After baking out the casting solvent, electron exposure modifies the resist.

Polymethyl methacrylate (PMMA) is a common positive resist used for high resolution patterning. As shown in Fig. 2.13, at low exposure doses the polymer chains will break into shorter chains, which are soluble in the commonly used developer methyl isobutyl ketone (MIBK). At higher exposure doses, the chains will cross-link and become insolubile in MIBK, resulting in a transformation of the resist from a positive to a negative character [17].

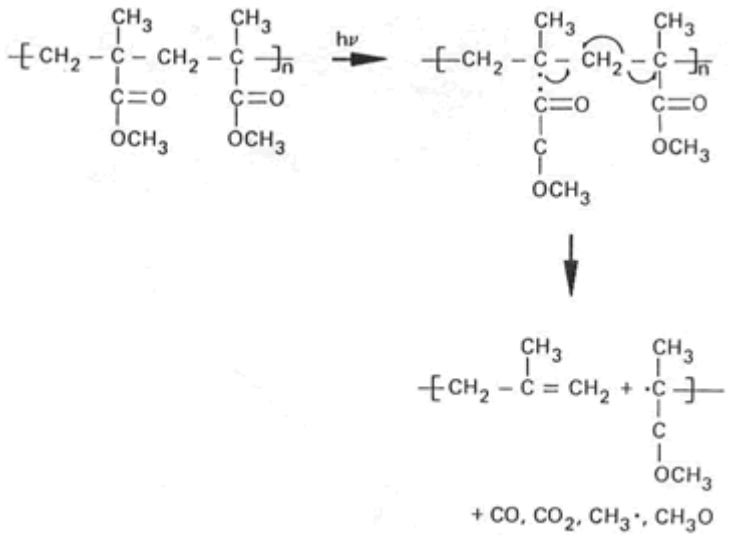

Fig. 2.13 Chemical transformation of PMMA under electron beam exposure.

Given the availability of technology that allows a small-diameter focused beam of electrons to be scanned over a surface, an EBL system does not need any mask. An EBL system simply "draws" the pattern over the resist wafer using the electron beam as its drawing pen, making the patterning process a serial process. The resolution in optical lithography is limited by diffraction, and this applies to electron lithography too. Although the short wavelengths of the electrons in the energy range used by EBL systems means that diffraction effects do not affect much the high resolution performance. However, the resolution of an electron lithography system may be constrained by other factors, and depends on several parameters such as the size and the energy of the electron beam, the type of resist, its thickness and the type of substrate. The development process might also influence the shape of the final pattern as well as

its resolution. Structures with sizes down to 5 nm have been made with electron beam lithography [17].

Dedicated EBL systems are typically operated at electron energies of 50 or 100 keV. In general, high electron energies results in a small electron probe which can be used for high resolution imaging and patterning. Electrons with high energies are also less sensitive to lens aberrations in the electron microscope as compared to electrons with lower energies (~1-10 keV). When the electrons hit the resist on top of the sample, they will interact both elastically (producing forward scattered electrons causing beam broadening) and inelastically (producing secondary electrons). When the electrons travel through the resist and hit the substrate they will also produce backscattered electrons from a depth of several micron into the substrate. The forward and the backscattered electrons will contribute to the resist exposure outside the scanned area. This is called the proximity effect and will degrade the pattern quality [17].

3. Study of defects

3.1 Disorder in graphene

Graphene is a remarkable material because of the robustness and specificity of the σ bonding, and it is very hard for alien atoms to replace the carbons atoms in the honeycomb lattice. Nevertheless, graphene is not immune to disorder and its electronic properties are controlled by extrinsic as well as intrinsic effects that are unique to this system. Among the instrinsic source of disorder it is possible to highlight surface ripples and topological defects. Extrinsic disorder can come about in many different forms: adatoms, vacancies, charges on top of graphene or in the substrate, and extended defects such as cracks and edges [8].

Graphene can be considered the extreme case of a soft membrane. Hence, it is subject to structural distortions of its structure either due to thermal fluctuations or interaction with a substrate. The disorder is due to the modification of the distance and relative angle between the carbon atoms because of the bending of the graphene sheet. In the presence of a substrate, elasticity theory predicts that graphene can be expected to adhere to the substrate in a smooth way. Hence, disorder in the substrate translates into disorder in the graphene sheet [8].

Structural defects of the honeycomb lattice are also possible in graphene and can lead to scattering. These defects induce long range deformations, which modify the electron trajectories.

Point defects, such as impurities and vacancies, lead to a finite elastic mean free path, and to an elastic scattering time.

Localized states can be defined at edges. Graphene edges can be strongly deformed, due to the bonding of other atoms to carbon atoms. Localized states can also be found near other defects that contain broken bonds or vacancies [8].

3.2 Engineering the conductivity of graphene with defects

It is common knowledge that defects always decrease the mobility of the carriers compared with the defect-free version because of the introduction of additional scattering sites: in some cases defects may increase the number of carriers. The latter effect is especially important here and leads to a strong conductivity rise, since for ideal graphene there are no carries at the Fermi energy [18]. Quantum mechanical transport calculations, as well as experimental studies, have shown a pronounced enhancement of the conductivity after insertion of defects. This fact can be attributed to the defect induced mid-gap states, which create a region exhibiting metallic behaviour around a vacancy defect. Furthermore, it has already been shown that a band-gap can be opened in graphene, and that it can be tuned as a function of carrier concentration [18].
The modification of the conductivity of graphene by implantation of stable defects is crucial for the creation of electronic junctions in graphene-based electronic devices.

Since it is possible to tune graphene's transport properties by inducing defects, it becomes of crucial importance to understand how vacancy defects can actually influence the electronic structure of graphene. When considering graphene as consisting of two sublattices, A and B, it is known that the effect of an impurity in the A sub-lattice is manifested in the B sub-lattice as well. A vacancy in the π-band, *i.e.* the absence of π orbitals at the impurity site, generates mid-gap states for the atoms in the B sub-lattice located in the neighbourhood of the vacancy [18]. The emerging mid-gap state suggests that the sub-lattice B becomes metallic in the presence of the vacancy in the A sub-lattice. Generalizing this behaviour to the case of a di-vacancy, with two adjacent vacancies of which one is in each sub-lattice, one expects the emergence of mid gap-states in both sub-lattices for atoms in the neighbourhood of the di-vacancy. This indicates that graphene becomes metallic in a neighbourhood of a di-vacancy. The length scale associated with the metallicity around the di-vacancy is of the order of a few lattice constants, which is due to the spatial power law decay of the influence from the impurity [18].

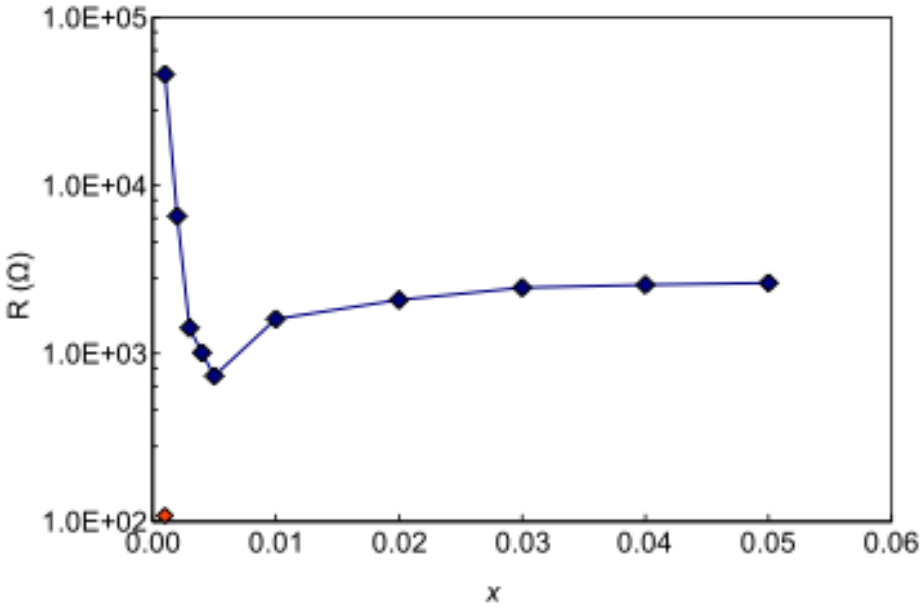

Fig. 3.1 Calculated resistivity of a single layer of graphene as a function of defect concentration [18].

Fig. 3.1 from a previous work carried out at Uppsala University, shows the result of a calculation for single C vacancies (the results are expected to hold also for other vacancy geometries). As the concentration of vacancies grows, the 0 K temperature resistivity decreases with at least one order of magnitude compared with the material containing no vacancies. In the concentration regime $\leq$ 0.5 % it is seen that the conductivity decreases exponentially with respect to the defects concentration. This is actually an expected result for regular semiconductors. For a larger concentration of vacancies, the resistivity slightly increases and appears to saturate close to a constant level for a defect concentration of 3-5 %. This behaviour can be seen as a transition from a semi-metallic regime with limited conductivity, to a regime of highly conductivity graphene. This transition, as said before, is driven by defects via the creation of mid-gap states. Once this regime has been fully established, the addition of further defects produces scattering centres which reduce the conductivity, resulting in a more conventional behaviour [18].

This aspect can become central if we want to use graphene in electronics, to build for instance logic gates. In this case the metal-insulator transition allows the gate to switch from on-to-off response and vice-versa, as required for a transitor.

3.3 Raman spectroscopy

As we already discussed in the paragraph 2.2.3, a suitable tool to study the formation of defects in mono- or multilayer graphene is Raman spectroscopy. This is due to a so-called “defect peak” D present in the graphite and graphene spectra. The D peak intensity increases as the amount of defects increases.

For a long time Raman spectroscopy has been used to study carbon-based materials due to the specific response to any change in carbon hybridization state, as well as the introduction of defects or foreign species. The effect of ion irradiation on highly oriented graphite samples has been studied with Raman spectroscopy by Dresselhaus et al. more than 20 years [19]. They observed that three regimes of behaviour can be achieved by evaluating the energy deposited into the sample during the collision cascade. At low fluences the disorder D line located at 1360 cm^{-1} starts to appear and its intensity grows quite linearly with the ion fluence. In this regime the peak is sharp and related with the appearance of pockets of disorder within ordered HOPG (Highly Oriented Pyrolytic Graphite). At intermediate fluences the first order Raman peaks start to broaden because of the percolation of single disorder domains. At these first two stages, generally, annealing to moderate temperatures will restore the primitive order. A final stage can be obtained by further increasing the damage, thus leading to an amorphous carbon sample [20].

A similar scenario can be assumed to occur also during ion irradiation of single and multi-layer graphene deposited on SiO_2, even if the threshold fluences between the mentioned three regimes are not known exactly in this case. Of course these threshold values depend on the mass and the energy of the irradiating ions [20].

4. Experimental

4.1 Production

The production of monolayer graphene can be performed in several ways, such as Chemical Vapour Deposition (CVD), decomposition of SiC, sonication or mechanical exfoliation from bulk graphite.

The force responsible for the binding between graphite layers is the Van der Waals force, which is much weaker in comparison to the strong covalent bonds that link the carbon atoms in each layer. Because of that, it is easy to break such a weak link between layers without destroying the layers themselves.

Novoselov *et al*. in 2004 achieved to observe, select and characterize graphene through the cleavage of graphite layers, with what they call "scotch tape method", where mechanically exfoliated graphite layers were deposited on a substrate.

Mechanical exfoliation, because of its simplicity, is actually the most used technique for producing monolayers with ease and reproducibility in table-top experiments.

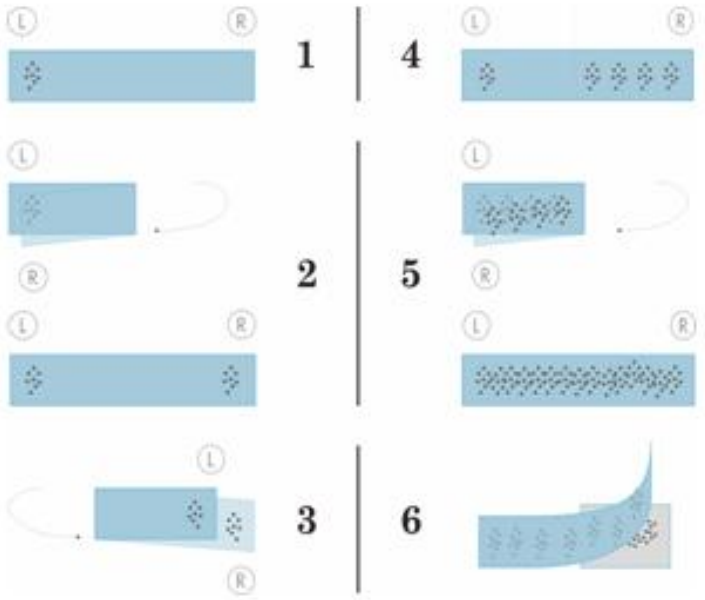

Fig. 4.1 Mechanical exfoliation technique for the production of graphene flakes.

Basically a Highly Oriented Pyrolytic Graphite (HOPG) sample is cleaved by using common scotch tape (Fig. 4.1), which removes a number of layers from the sample surface at a first peeling. This slim stack is then thinned down by folding the tape back and forth several times, until an homogeneous distribution of flakes is obtained onto the surface of the tape. At this point, the result of the exfoliation is in part transferred to a suitable substrate, usually a Si wafer with a 300 nm SiO_2 layer on top of it.

4.2 Characterization (detection and identification)

4.2.1 Light optical microscopy

In order to detect a graphene flake on the silicon dioxide surface, a standard optical microscope can be used. In this work an OLYMPUS AX70 is used in reflection mode.
The substrate is introduced in the LOM and first scanned by eye with a 20x magnification until a graphene candidate is spotted. When a candidate is detected, it is opportune to take several pictures of it at different magnifications, in order to be able to find the flake later again for further analysis.
Fig. 4.2 shows a LOM image of a graphene flake at magnification a) 200x and b) 20x. As we can see from the image, thin flakes can be distinguished from thicker flakes by their different colour and contrast: the thinner the flake, the less the contrast with respect to the substrate. Hence, dark flakes represent multilayer graphene (or bulk graphite when the colour turns to yellow), and monolayer flakes can be almost invisible. Once a graphene flake is detected, it is opportune to note the position of the flake with respect to the whole substrate with a schematic diagram. This allows a much easier retrieval of the flake position in other setups or instruments where the thin graphene flake would not be visible.

a)

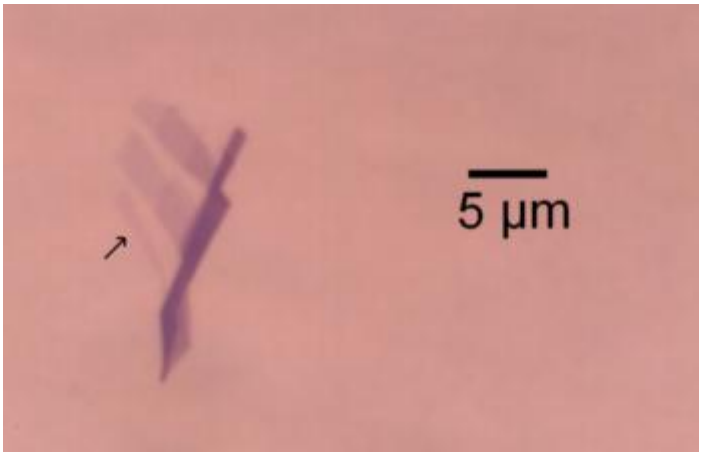

b)

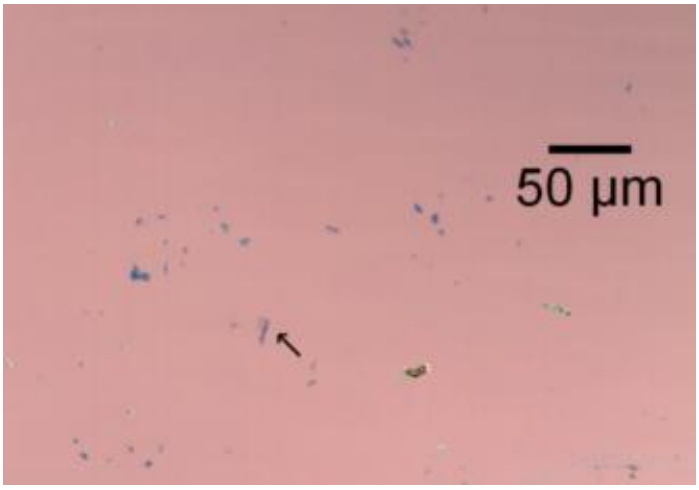

Fig. 4.2 LOM images of graphene flakes at 200x magnification (a) and 20x magnification (b). The colour of the flake changes depending on its thickness. The flake indicated by an arrow is a monolayer graphene.

4.2.2 Atomic Force Microscopy

The use of an atomic force microscope allows a direct and reliable study of the wafer surface. In this work an AU04 AFM (XE 150) in non-contact mode has been used to estimate the thickness of flakes deposited on a silicon wafer without damage for either tip or sample. Due to the interaction between the tip and the flake, unevenness of the substrate and bond between the carbon layer and the substrate, the results of the measurements are affected and nevertheless the thickness of a monolayer is known to be 0.335 nm, the AFM measures an effective thickness of approximately 1 nm.
Fig. 4.3 shows an AFM image of the flake in Fig.4.2.

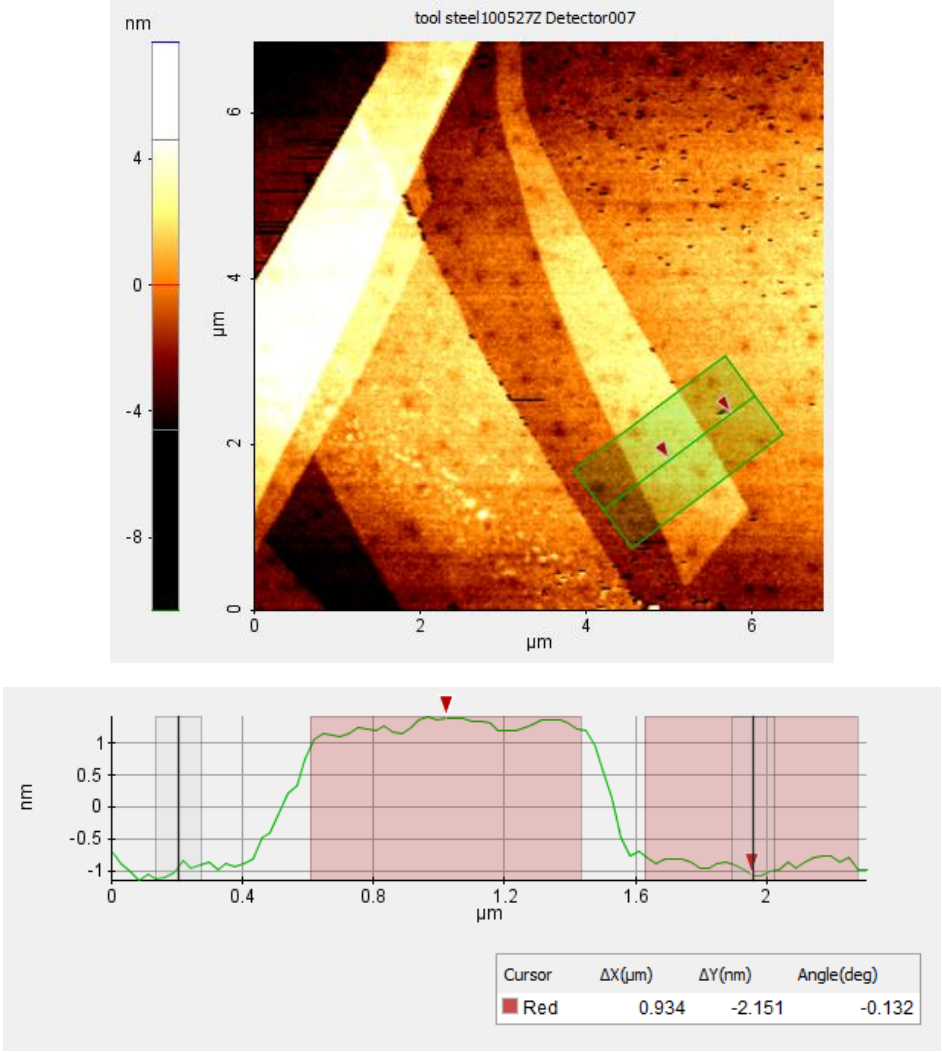

Fig. 4.3 AFM image of a graphene layer deposited on SiO_2. The flake appears lifted from the surface of about 2 nm.

Although further analysis proved that the flake is a monolayer, the measured thickness by AFM is around 2 nm.

Another information that we can extract from the AFM topography, is the roughness of both the substrate and the sample. It is also possible to check the status of the surface since any deformation will be reflected on the graphene.

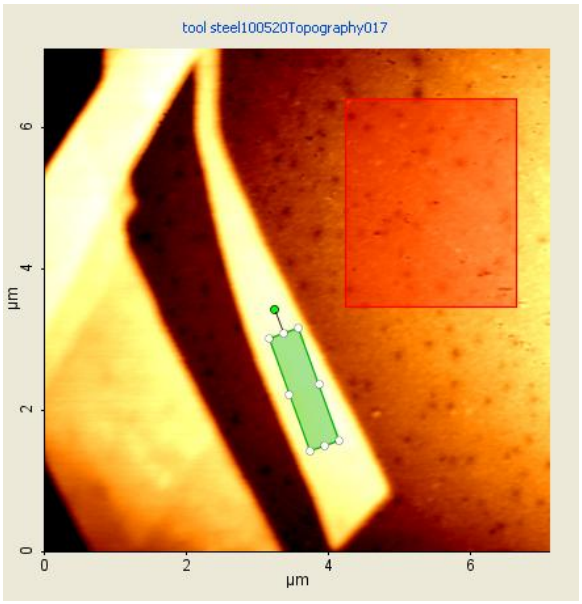

Statistics

Region	Min(nm)	Max(nm)	Mid(nm)	Mean(nm)	Rpv(nm)	Rq(nm)	Ra(nm)	Rz(nm)	Rsk	Rku
Red	-2.564	2.431	-0.066	0.291	4.996	0.807	0.686	4.570	0.033	2.253
Green	**3.256**	**4.361**	**3.809**	**3.933**	**1.105**	**0.220**	**0.176**	**1.067**	**0.597**	**2.995**

Fig. 4.4 AFM image of graphene on SiO_2. The image reports an estimate of both the flake and the substrate roughness.

The flake in Fig. 4.4 shows a roughness of about 0.180 nm, while the roughness of the surface is calculated to be about 0.7 nm. It should be noted that those values are an average value taken from a small area of the sample (the scanned part or a even smaller part selected after scanning) compared with the entire substrate, so those numbers don't refer to the whole substrate or the whole flake in absolute way, and the roughness may slightly change depending on the region under study.

4.2.3 Raman spectroscopy

The spectra taken in this work have been acquired with a 514 nm green laser light with a spot size of the order of a few microns. To avoid extensive heating of the sample and beam damage, only 10% of the full laser power (20 mW) was used for the analysis.
In Fig. 4.5 the Raman spectrum of the flake presented in Fig 4.2 (LOM image) is plotted.
The shape of the 2D peak and its height with respect to the G peak indicates the flake to be a single layer. The D peak (disorder peak) is slightly visible which indicates a small

amount of defects present in the flake, most probably induced during the production process and from the interaction of the graphene flake with the substrate.

Another example is shown in Fig. 4.6 and 4.7, where the asymmetry of the 2D peak and its height with respect to the G peak, suggest that the flake is not a single layer graphene. In all the Raman spectra of contacted samples a strong background can be seen (Fig. 4.6). It is not clear if the background is constant or not since it decreases to zero around the origin, most likely because of the filter used to suppress the signal from the Rayleigh scattering (see paragraph 2.2.3). The background is a significant fraction of the peak intensities and makes the interpretation of the peak ratio questionable. Its physical origin could be attributed to the gold contacts. It is known that gold nanoparticles can enhance the Raman signal and, in this case, they might amplify a fluorescent signal from the sample, the substrate or contaminants (residuals from the scotch tape or the PMMA or the developer)[*].

The peak centred around 500 cm^{-1} visible in all the spectra is characteristic of the SiO_2 substrate underneath the flake.

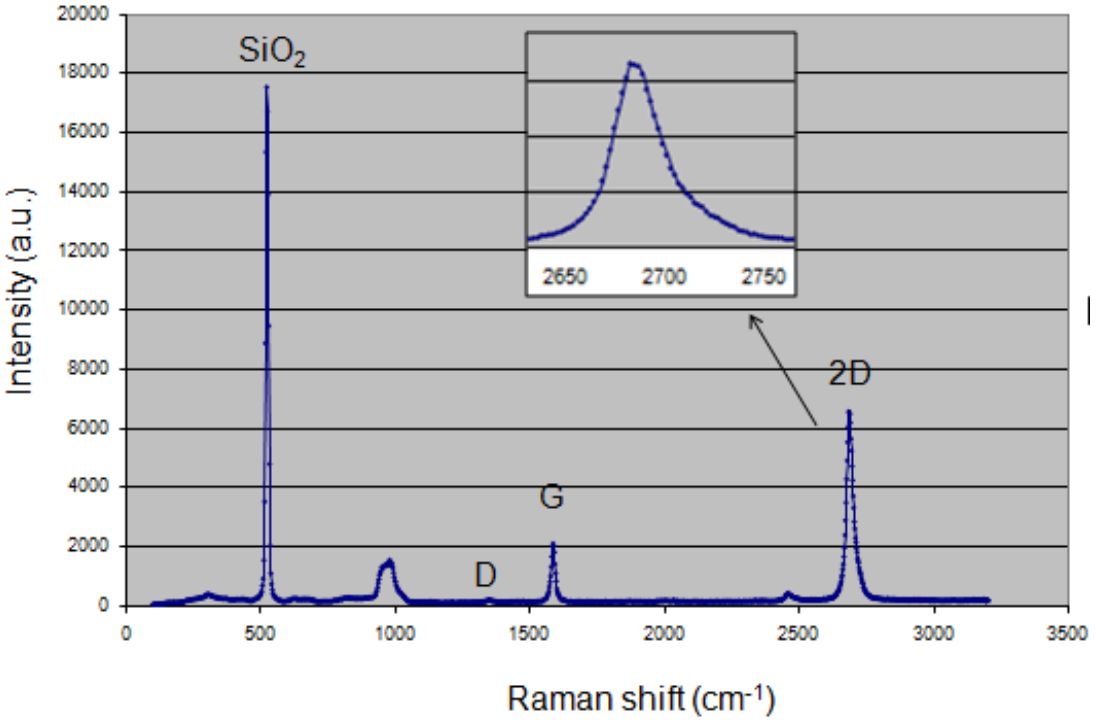

Fig. 4.5 Raman spectrum of a monolayer graphene flake.

*Tomas Edvinsson, private communication.

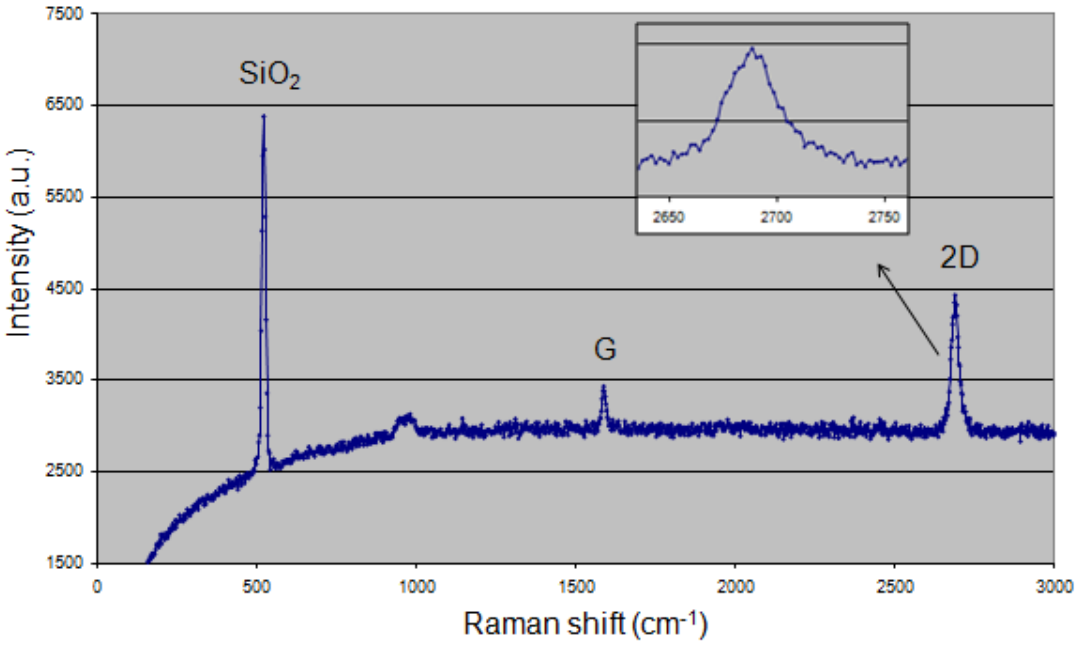

Fig. 4.6 Raman spectrum of a contacted graphene flake. The asymmetry of the 2D peak suggests that the flake is not a single layer graphene.

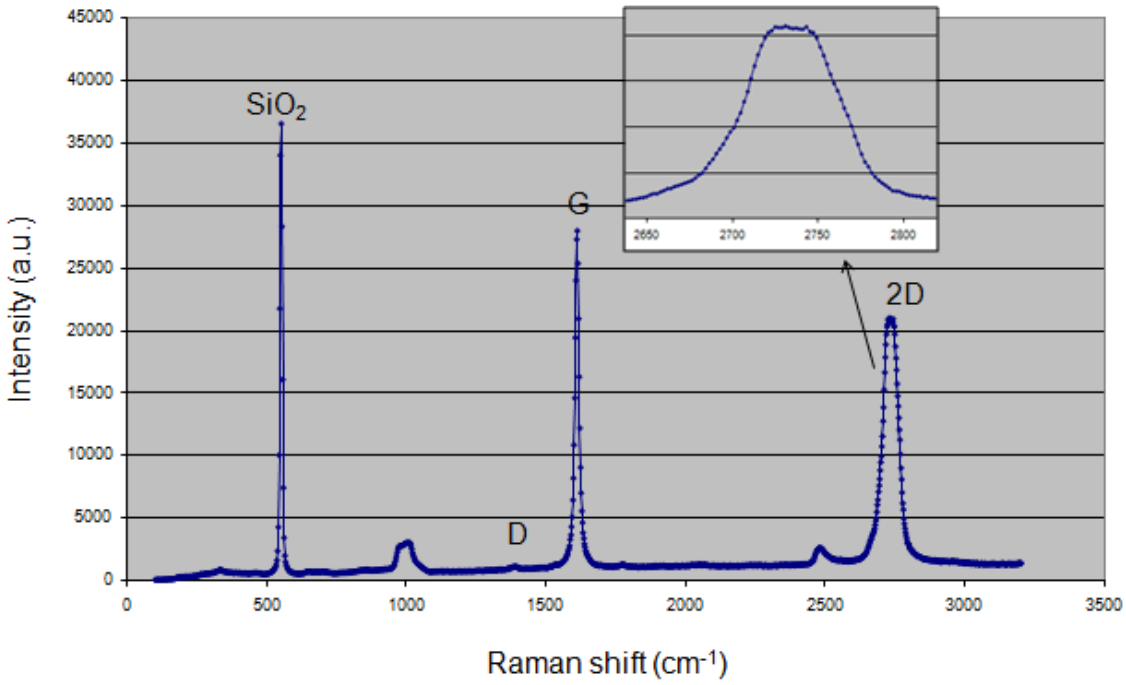

Fig. 4.7 Raman spectrum of a multilayer graphene flake. The asymmetry of the 2D peak and its height with respect to the G peak display that the flake is not single layer graphene.

4.3 Electron Beam Lithography

A typical electron beam lithography (EBL) system consists of the following parts: 1) an electron gun that supplies the electrons; 2) an electron column that focuses the electron beam; 3) a mechanical stage that positions the wafer under the electron beam; 4) a wafer handling system that automatically feeds wafers to the system and unloads them after processing; and 5) a computer system that controls the equipment [17].

In this work EBL has been performed in a Scanning Electron Microscope (SEM) equipped in a Focused Ion Beam (FIB) system. The patterns (pads and wires) are designed by drawing the patterns manually and expose the area with the electron beam.

The EBL process in the present work can be summarized in the following steps (see also paragraph 2.3, EBL):

- Spin coating of the silicon substrate and graphene flake with PMMA of approx. 150 nm thickness: 1 ml of PMMA is deposited by using a syringe on the wafer which is successively spin coated for 5 sec at 500 rpm increasing to 4000 rpm for 55 sec. Then the substrate is baked on a hot plate at 170 °C for 1 min in order to evaporate the solvent.
- The pads and the leads in Fig. 4.8 are manually drawn by using the drawing tools available in the FIB software (the original design planned four pads for possible Hall measurements; for our measurements two pads would be enough). An acceleration voltage of 30 kV is used and the probe current has been measured to about 100 pA. From previous experience from EBL in an ESEM, the electron dose should be roughly 270 $\mu C/cm^2$ in order to fully expose the PMMA. The probe current and the dose can be converted to a patterning time which in this case is 0.02185 $s/\mu m^2$.
-

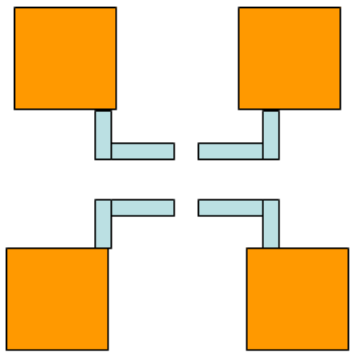

Fig. 4.8 Sketch of the pads patterned by EBL.

- Development of the exposed area by using a suitable chemical solution (*developer*) which removes the region of PMMA previously exposed to the electron beam. The quality of the resulting patterns is checked in a LOM.
- Evaporation of the sample in a vacuum chamber. The technique used is called *resistive evaporation*, in which the deposited material is put in tungsten boats which are clamped between two electrodes inside the vacuum chamber of the evaporator. During the evaporation, a large current (up to 60-70 A) is fed through the tungsten boat which will become so hot that the metal inside starts to evaporate. An optimal value for the pressure in the chamber is in the low 10^{-6} or 10^{-7} mbar range, usually reached by pumping overnight. This low pressure is needed in order to limit the amount of impurities that could be included in the contacts during the evaporation. A Ti adhesion layer of 10-20 nm is deposited first, followed by deposition of 70-100 nm of Au from tungsten boats. The sample is rotated during deposition to achieve homogenous coverage.
- Removal of the PMMA from the regions not exposed. The sample is soaked in acetone for about 1 hour. When the metal on top of the PMMA starts to peel off, the sample is rinsed and blow dried with nitrogen gas. The patterns are checked in the LOM in order to see if the lift-off was completed with success [17].

The typical contacting device of graphene consists of big external pads and smaller pads (Fig. 4.8) that connect the graphene flake to the big pads. Since it is not always possible to locate the exact position of the flake in the SEM, it is possible to do reference measurements by using a LOM. Typically, the distance from the flake to the edge of the substrate is measured. In this way the flake can be approximately located on the substrate once placed in the SEM chamber. First, the bigger pads are designed at a safe distance from the flake. Once the bigger pads are completed, the sample is placed back in the LOM and the distance from the flake to the pads is now measured. The smaller pads are then designed, and the flake is connected in this next exposure step. The EBL process is repeated twice in order to draw the whole contact device. Due to limitations in the precision of the placement of the pattern and also due to the difficulty in determining the position of the flake when coated with PMMA, it can happen that one or both sides of the sample are not connected to the pads. In this case the EBL process has to be repeated again. In worst case, the pads might accidently be patterned on top of a flake and will then fully reveal the entire flake. In such cases, the PMMA will have to

be removed and new PMMA should be respun. In this work, four large pads were deposited. With this device, *in situ* measurements could be performed in a FIB by grounding one pad and contacting another one with a conductive nanomanipulator tip connected to a multimeter. For the ion irradiation experiments in the Tandem accelerator, the sample had to be mounted on a chip holder connected to a multimeter (see also paragraph 5.1.3). To provide electrical connections, the pads had to be attached to fine gold wires by means of conductive silver paint. Since the big pads are only a few micron apart, the risk of covering the sample with silver paint is great. To eliminate the risk of short-circuits, additional pads were deposited by spin coating PMMA and then scratching it away with a fine glass needle to create irregular pads of few millimeter in size extending from the big pads to the edge of the wafer. Part of these "scratched" pads can be seen in Fig. 4.9 and Fig. 4.10.

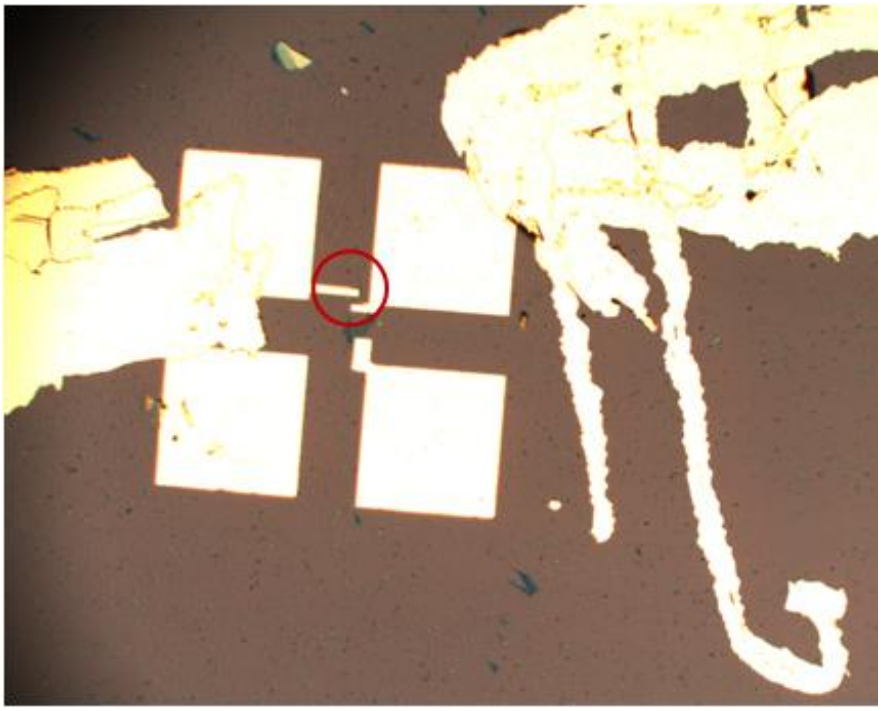

Fig. 4.9 LOM image of electrical contacts on graphene deposited by EBL. On the side we can see the scratches made by hands where more gold has been deposited on them The size of the square pads is 100 μm^2 each.

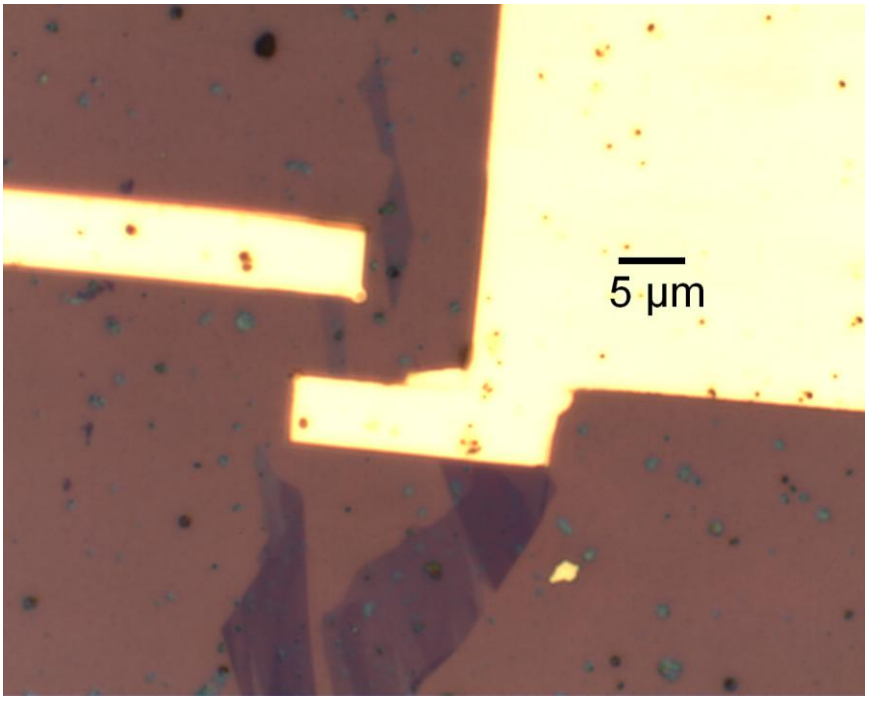

Fig. 4.10 Zoom of fig. 4.9. We can see the graphene flake contacted between the gold bars.

5. Ion irradiation

5.1 Ion physics

5.1.1 Focused Ion Beam

FIB systems have been produced commercially for approximately twenty years, primarily for large semiconductor manufacturers. FIB systems operate in a similar fashion to a SEM except, rather than a beam of electrons and as the name implies, FIB systems use a finely focused beam of ions (usually gallium) that can be operated at low beam currents for imaging or high beam currents for site specific sputtering or milling. The gallium (Ga+) primary ion beam hits the sample surface and sputters a small amount of material, which leaves the surface as either secondary ions (i+ or i-) or neutral atoms (n^0). The primary beam also produces secondary electrons (e^-). As the primary beam rasters on the sample surface, the signal from the sputtered ions or secondary electrons is collected to form an image. The FIB technique is particularly used in the semiconductor and materials science fields for site-specific analysis, deposition, and ablation of materials.

The microscope used in this thesis is a FEI Strata DB235 FIB/SEM equipped with a field emission gun (Fig. 5.1). It consists of an electron beam and an ion beam. The electron beam column is vertically oriented and the electron energies can be varied between 0.2 and 30 keV. This beam can be used for acquiring high resolution SEM images, electron beam induced deposition and for acquiring information about the chemical composition of the sample together with the Energy Dispersive X-ray Spectroscopy (EDS) detector. The ion beam column is tilted to an angle of 52° with respect to the electron column. It consist of positively charged Ga ions accelerated to energies between 5 and 30 keV. The beam can be used to generate secondary electrons and ions which can be used to form images [17].

The ions are emitted from a liquid metal ion source, consisting of a W filament with a reservoir close to it filled with Ga. When the filament is heated, the Ga becomes liquid and wets the W surface. An extractor voltage of typically 12 kV is applied in order to

extract the ions from the tip. The extractor voltage is typically held at a constant value whereas a suppressor voltage is used to generate emission current from the ion source. The emission current is typically held constant at 2.2 µA for the Strata DB235. The source is generally operated at low emission currents to reduce the energy spread of the beam and to yield a stable beam [17].

Fig. 5.1 Picture of the FIB at MSL lab, Ångström laboratory.

5.1.2 Tandem accelerator

For the ion irradiation of the sample, the accelerator mass spectrometry (AMS) system at Uppsala University was used.

The Tandem Van der Graaf machine (Fig. 5.2) (Ion Physics group, Uppsala University) is a type of particle accelerator in which the high voltage at the terminal (nominal value = 6 MV) is used twice to increase the energy of the injected ions. Negative ions are accelerated by the positive potential of the terminal. When reaching the terminal, electrons are stripped off in a thin foil or gas, and a second accelerator takes place by repulsion back to ground potential (the tandem principle). The high energy obtained after the acceleration allows for a unique identification of each ion by conventional nuclear detection. The charge distribution of a beam of ions passing through a gas foil depends on the velocity and type of the ions and on the stripper composition. In order to have the highest possible count rate at the detector, the charge state has to be chosen so

to be the most probable one. However, this choice is limited by other factors such as the magnetic rigidity of the analyzing magnet and the possible presence of interfering molecular fragments.

At the exit of the accelerator tube. The beam is deflected through the 90° double-focussing fringing analyzing magnet and deflected through the 30° switching magnet before entering the 20° cylindrical electrostatic deflector and the detection region . The bending radius and the limited maximum value of the magnetic field (B = 1.6 T) in the analysing magnetic strength restrict the charge state that can be selected at a fixed energy of the ions [21].

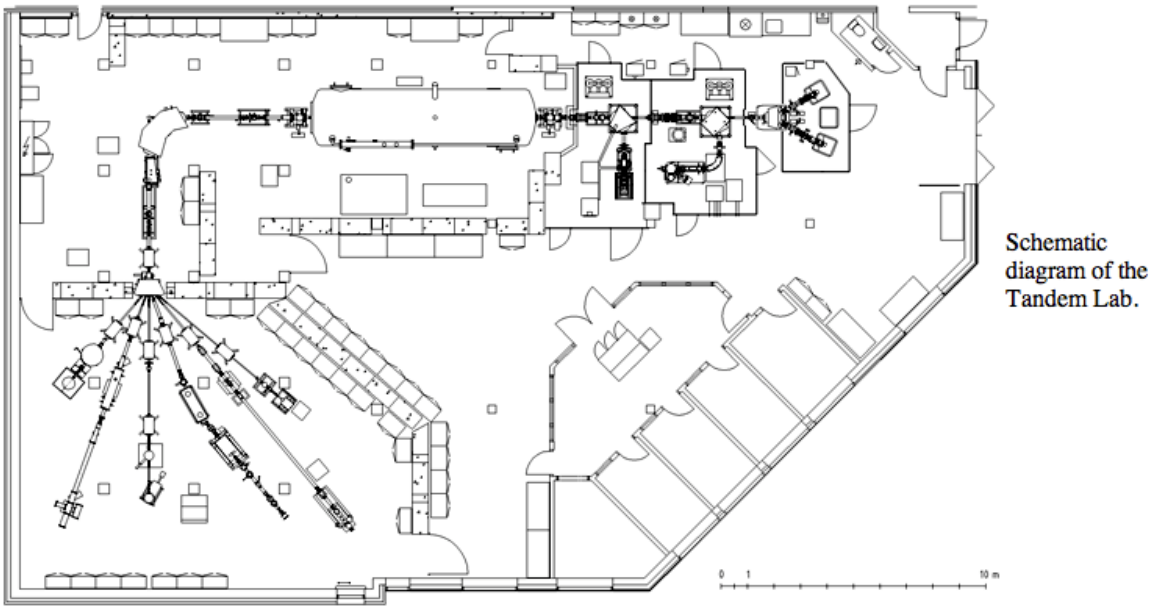

Fig. 5.2 Plant of the Tandem Laboratory at Uppsala University.

5.1.3 Sample preparation

Both bare (as-exfoliated) graphene flakes and contacted graphene flakes were used. The contacted samples were placed on a special sample holder for chips (Fig. 5.3). The electrical connections between the gold contacts on the sample and the sample holder were made by attaching thin gold wires from the sample to the legs of the chip holder with conductive silver paint (Fig. 5.4).

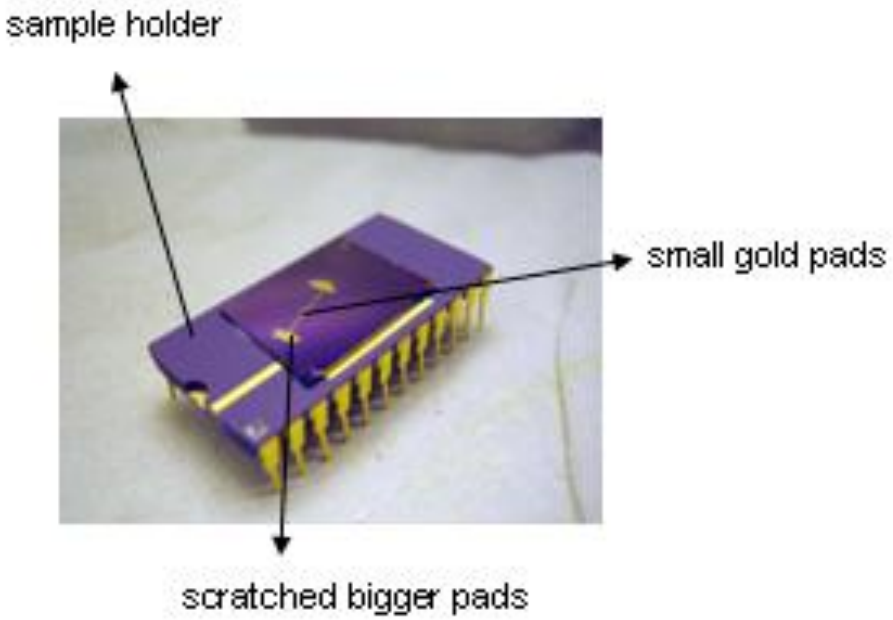

Fig. 5.3 Chip sample holder. The substrate is placed on the top of it.

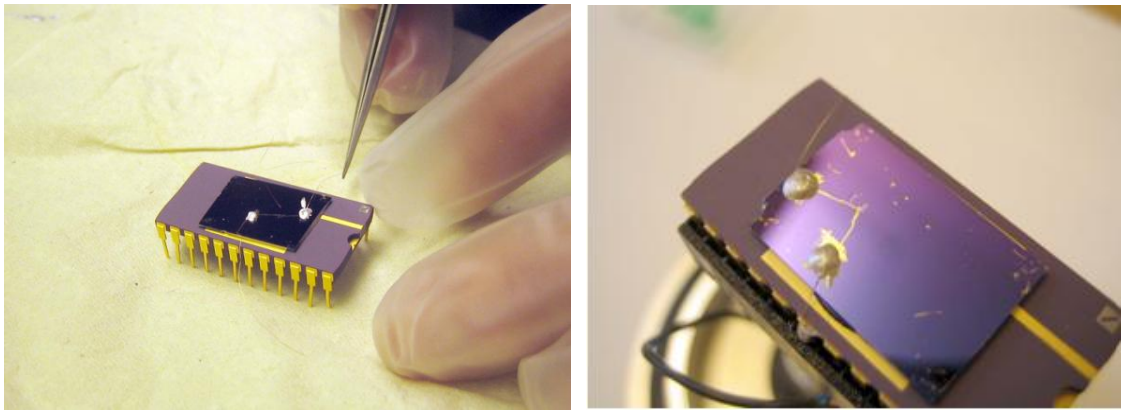

Fig. 5.4 Wire contacting process of the sample with thin gold wires (left). Closer view on the right.

The sample holder is then mounted on a plate. In order to avoid irradiation of the whole substrate and sample holder, a metallic shield was placed on top of it (Fig. 5.5). The presence of the shield was deemed necessary after the first irradiation experiment (with C ions) showed an anomalous I-V curve, excessive outgassing and heating of the sample. More details about this first experiment are described in paragraph 6.1.

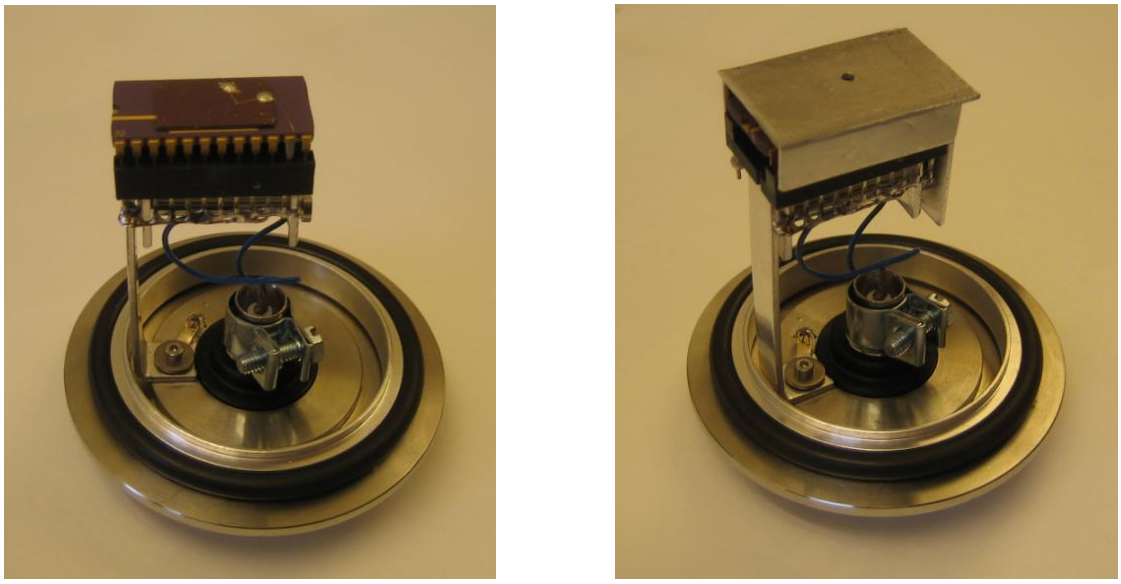

Fig. 5.5 The image shows a picture of the plate where the sample is placed before it is inserted inside the chamber. On the right side we can see the shield deposited on it.

The chamber, where the sample is placed during the irradiation (Fig. 5.6), is pumped down to 10^{-6} mbar, and the vacuum is monitored by a security system that shuts down the irradiation if the vacuum drops below a certain value.

The ion irradiation is manually switched on and off by means of a shutter in front of the sample holder, and the working power/current can also be set to the value of choice before every irradiation.

Fig. 5.6 Insertion of the sample into the chamber. Note the size of the instrument.

5.1.4 Software and electrical measurements

The electrical measurements have been carried out *in situ* during irradiation. A *Keithley 6430* was used as source-meter (Fig. 5.7). A script was written by H. Jafri with LabView to plot and record the measurements during irradiation.

Fig. 5.7 Data acquisition desk. The source-meter is placed on the right of the computer screen.

5.2 Stopping and Range of Ions in Matter simulation

Stopping and Range of Ions in Matter (SRIM) is a group of computer programs which calculate the interaction of ions with matter, including the stopping and range of ions (up to 2 GeV/amu) into matter using a quantum mechanical treatment of ion-atom collision. The ion and atom have a screened Coulomb collision, which includes exchange and correlation interaction between the overlapping electron shells. The ion has a long range interaction that creates electronic excitations and plasmons within the target. These are calculated from the target collective electronic structure and interatomic bond structure when the calculation is set up. SRIM is based on a Monte Carlo simulation method, namely the binary collision approximation with a random

selection of the impact parameter of the next colliding ion. The original program was developed by James F. Ziegler and P. Biersack in 1983 [22].

Transport of Ion in Matter (TRIM) is the most comprehensive program included. TRIM accepts complex targets made of compound materials with up to eight layers, each of different composition. It will calculate both the final 3D distribution of the ions and also all kinetic phenomena associated with the ion energy loss: target damage, sputtering, ionization, and phonon production.

Fig. 5.8 shows an image of the TRIM's setup window.

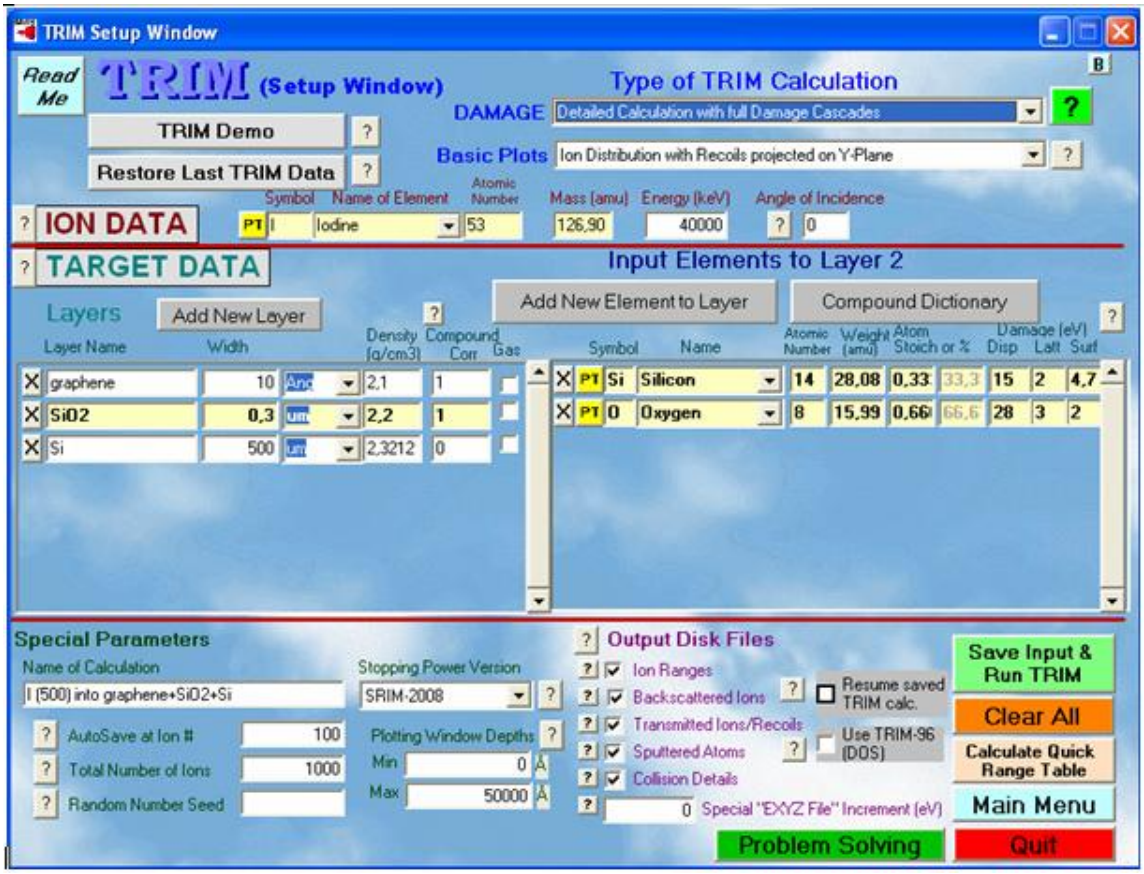

Fig. 5.8 Image of a TRIM's setup window.

The calculation simulates the irradiation of a graphene layer on top of a silicon wafer with a thin layer of silicon dioxide in between them. The ion chosen for irradiation is Iodine at 40 MeV, according to the experiment. In the following images the main results of the calculation are reported.

As we can see from the simulation, the penetration depth of the investigated system is about 10 μm. Other calculated parameters can be seen in the right-chart in Fig. 5.9.

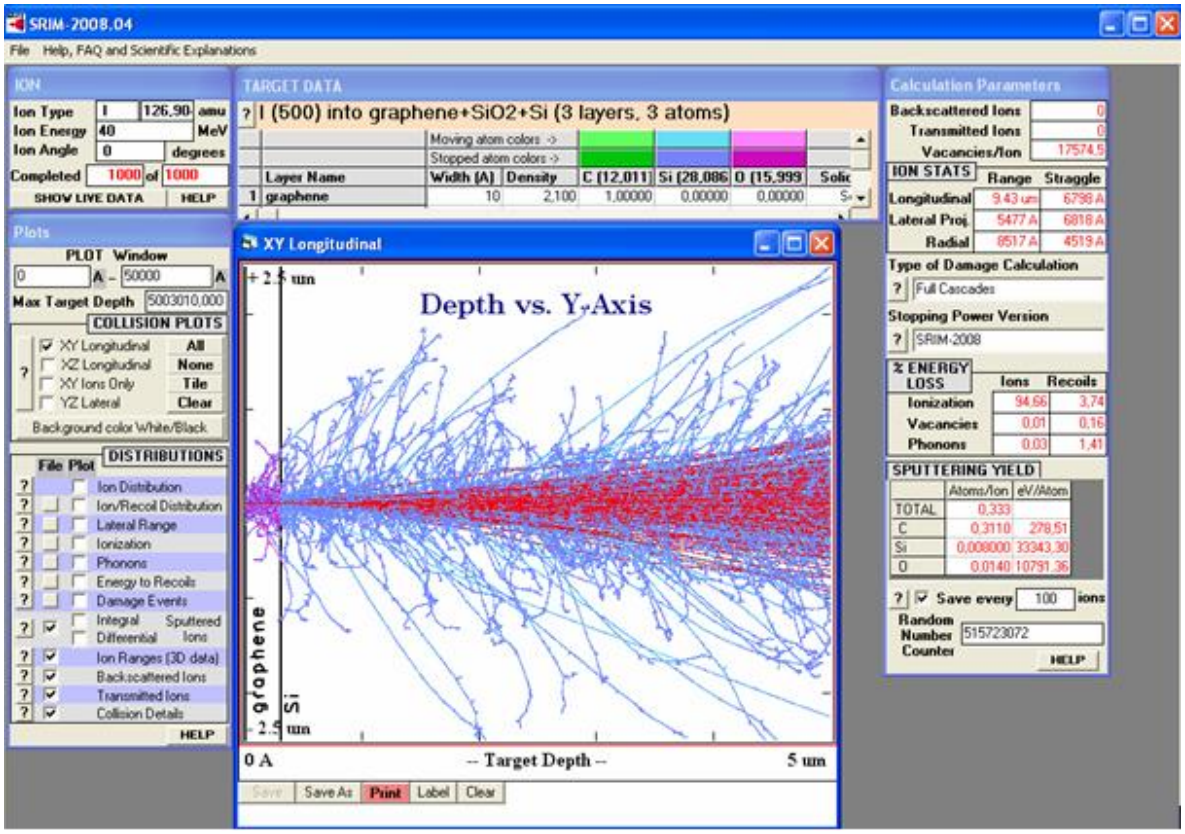

		Moving atom colors ->				
		Stopped atom colors ->				
	Layer Name	Width (A)	Density	C (12,011)	Si (28,086	O (15,999
1	graphene	10	2,100	1,00000	0,00000	0,00000
2	SiO2	3011920929	2,200	0,00000	0,33333	0,66667
3	Si	5000000	2,321	0,00000	1,00000	0,00000
	Lattice Binding Energy			3	2	3
	Surface Binding Energy			7,41	4,7	2
	Displacement Energy			28	15	28

Fig. 5.9 Output window of the TRIM analysis (top). Summary table of main results on the right.

The following graphs (Fig. 5.10-5.13) show the results of the simulation and some of the information that is possible to achieve.

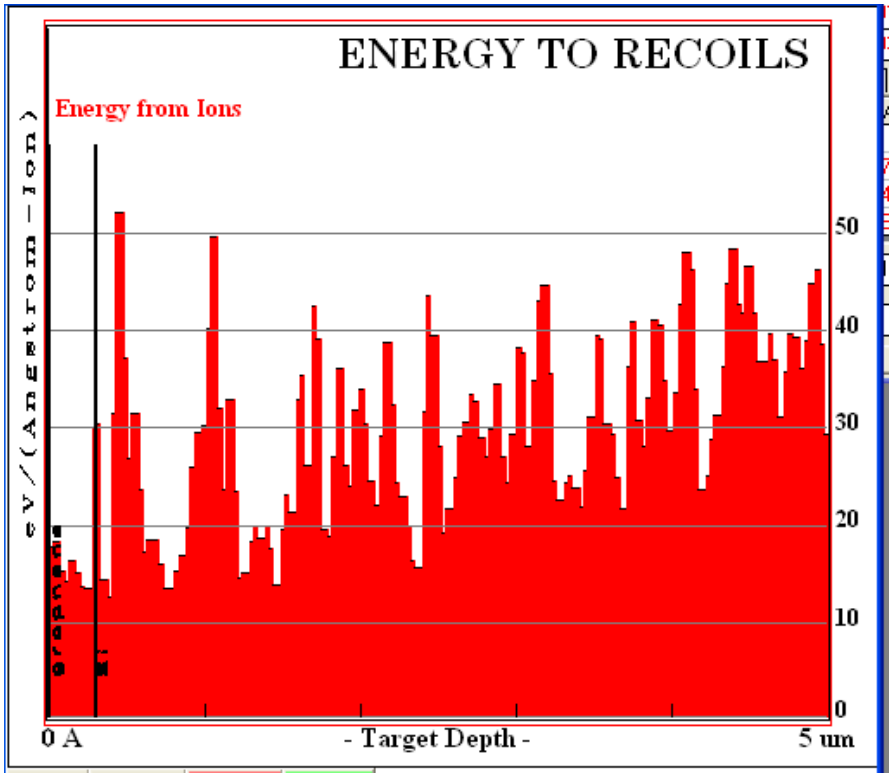

Fig. 5.10 Energy to recoils (from ions).

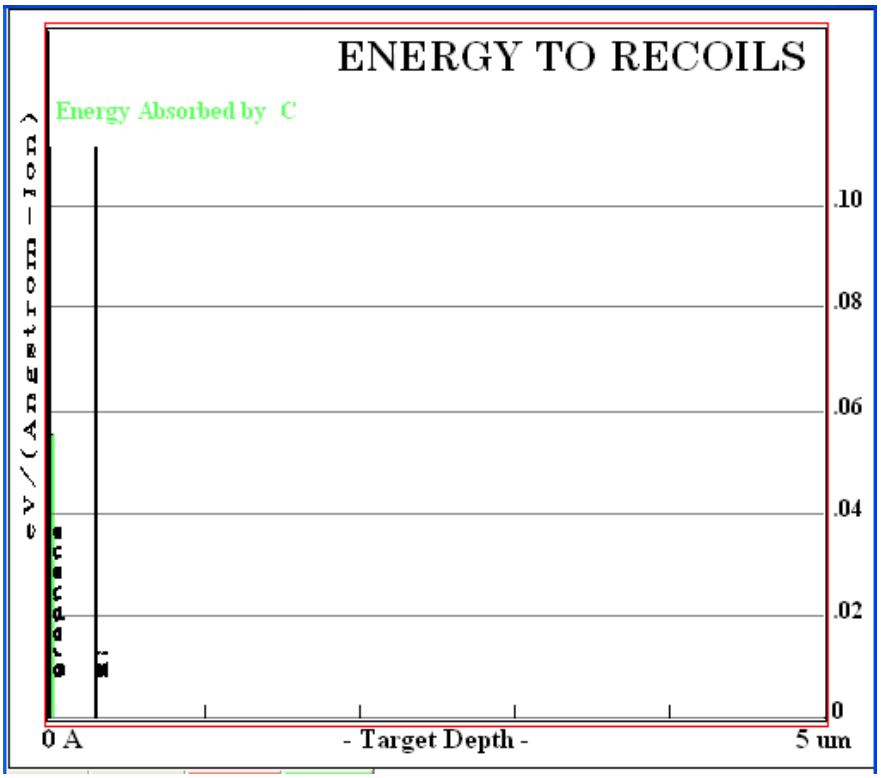

Fig. 5.11 Energy absorbed by C atoms.

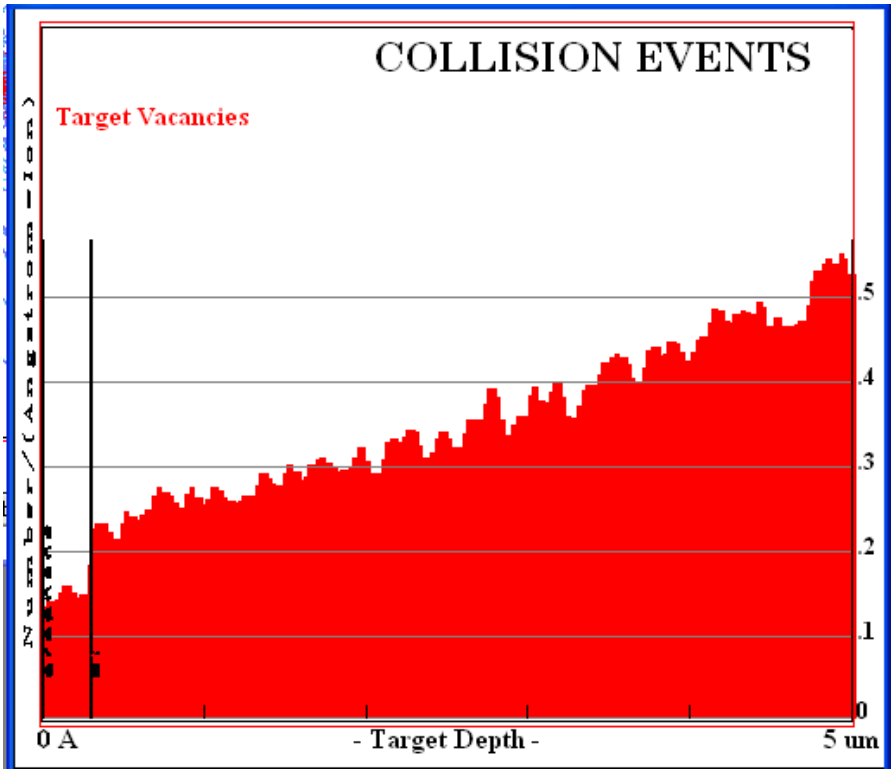

Fig. 5.12 Collision events (Target Vacancies).

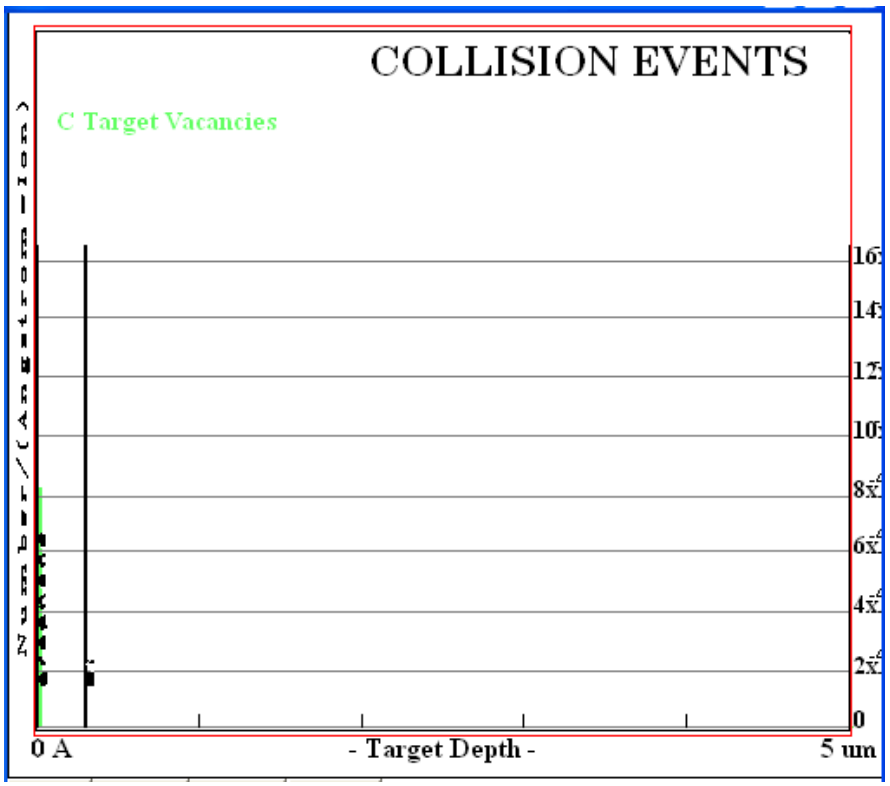

Fig. 5.13 Collision events (C Target Vacancies).

5.3 Experimental settings

Three experiment sessions have been performed.

In the **first experiment**, a contacted graphene flake was irradiated at the Ion accelerator at the Tandem Lab with 12 MeV C^{3+} ions and a beam current of 100 nA/cm^2. The purpose of this first experiment was to test the contacting device and assess the feasibility of *in-situ* electrical measurements. It also served as a benchmark for determining the importance of several experimental parameters during irradiation such as ion species and energy, vacuum level, specimen mounting and in the determination of which environmental factors have to be taken into account.

In the **second experiment**, both contacted and as-exfoliated graphene has been irradiated. For the as-exfoliated samples I^{7+} at 40 MeV was used at different driving currents (0.1nA/cm^2, 1nA/cm^2, 10nA/cm^2) for 10 s each sample. The distance between ions in the sample has been estimated to be respectively 335 nm, 106 nm, and 33.5 nm. Protons were used to irradiate a contacted sample which was electrically characterized *in situ* during irradiation. The sample has been irradiated several times.

In the **third experiment**, a contacted graphene flake was irradiated by FIB with Ga^+ ions at 30 kV, 1 pA current and a overlap of ions in the sample of 0%. *In situ* electrical measurements during irradiation were taken.

6. Results and discussion

AFM, Raman spectroscopy and electrical characterization have been carried out on graphene flakes before and after irradiation.

6.1 Atomic Force Microscopy

AFM is a good tool to estimate the thickness and the topography of a graphene flake. However it turned out not to be the optimum tool to investigate structural changes on graphene flakes after ion irradiation. Some defects are visible on the flakes, but an accurate observation of the images reveals that the same defects can be seen on both before- and after irradiation images (Fig. 6.1 and 6.2). Hence, no effect attributable to the irradiation can be observed by AFM. The reason for this might be that the resolution of the AFM is about 5 nm, which is much bigger than the size of a single atomic defect vacancy. Furthermore, the heavy presence of contaminants makes it difficult to detect the dislocations of the surface due to the impact of the ions.

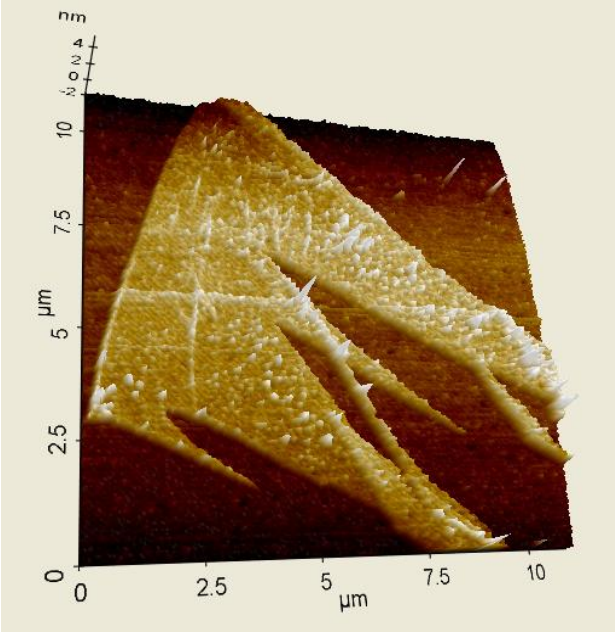

Fig. 6.1 AFM image of sample G13, flake2, before irradiation.

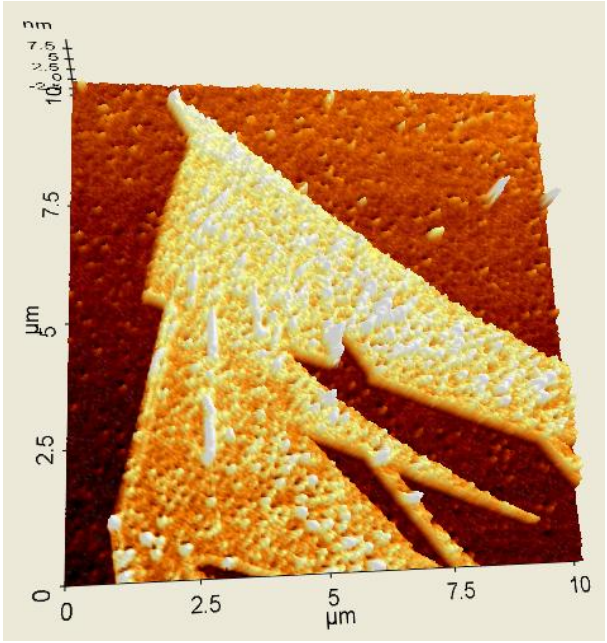

Fig. 6.2 AFM image of sample G13, flake2, after irradiation.

These contamination peaks can be up to a few µm wide and a few nm high, giving rise to an apparent surface roughness that is much higher than what clean graphene would give.

It has to be mentioned that the different colour of the images is due to the software setting and has nothing to do with the results. Also, it has to be taken into account that the topography map given by the AFM analysis, is a result of the interaction force between the tip and sample and could be affected by many factors as the laser resonance frequency, the exact distance between tip and sample, the goodness of the feedback loop, etc. Those parameters might be different for different scanning sessions, meaning that a small overall change in the images does not necessarily indicate a real change in the sample. Furthermore, for the same reason, some artefacts can occur during the scanning showing a topography feedback that doesn't correspond to the real situation.

It also has to be mentioned that the majority of the AFM images show some peaks, both on the flake and on the substrate, with a typical height ranging from few nm to few 10 nm. The origin and composition of those peaks is still unknown, but one possibility is that they are some glue residuals left from the exfoliation process.

It is imperative that the source of this contamination is identified and suppressed. One likely candidate would be glue residuals from the scotch tape used during mechanical exfoliation. Cleaning a freshly cleaved sample with different solvents or a mild plasma treatment might be of help. Nevertheless, cleaning procedures performed on the graphene flakes during previous attempts did not give the wanted results. Another source of contamination could be the EBL process (residuals of PMMA, developer, solvents or contaminations from the additional handling). However the contamination was detected also on non-contacted as-exfoliated flakes. Another point to consider is whether the effect of ion bombardment would be visible on the substrate used. The idea to use AFM came from the results of a previous study from Compagnini *et al*. which reports the change in the morphology of single layers with respect to the SiO_2 substrate at different irradiation fluences studied by AFM [20].

6.2 Raman Spectroscopy

Raman spectroscopy, an excellent tool for the detection of monolayer graphene, also provides some useful information about the change in the structure of the graphene flake due to the change in defect density. Nevertheless, the information obtained by Raman spectroscopy is qualitative, and cannot provide any quantitative information about the amount of defects or their structure.

Fig. 6.3 and 6.4 plot Raman spectra of one of the investigated flakes before and after irradiation by the Tandem ion accelerator.

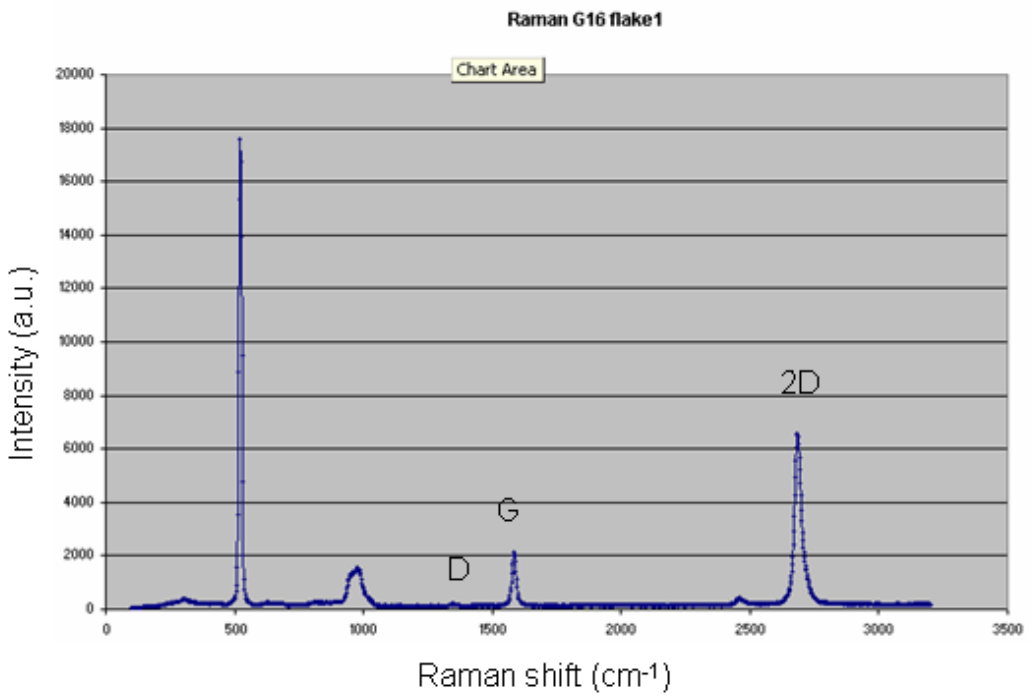

Fig. 6.3 Raman spectrum of a graphene flake on SiO_2, before irradiation.

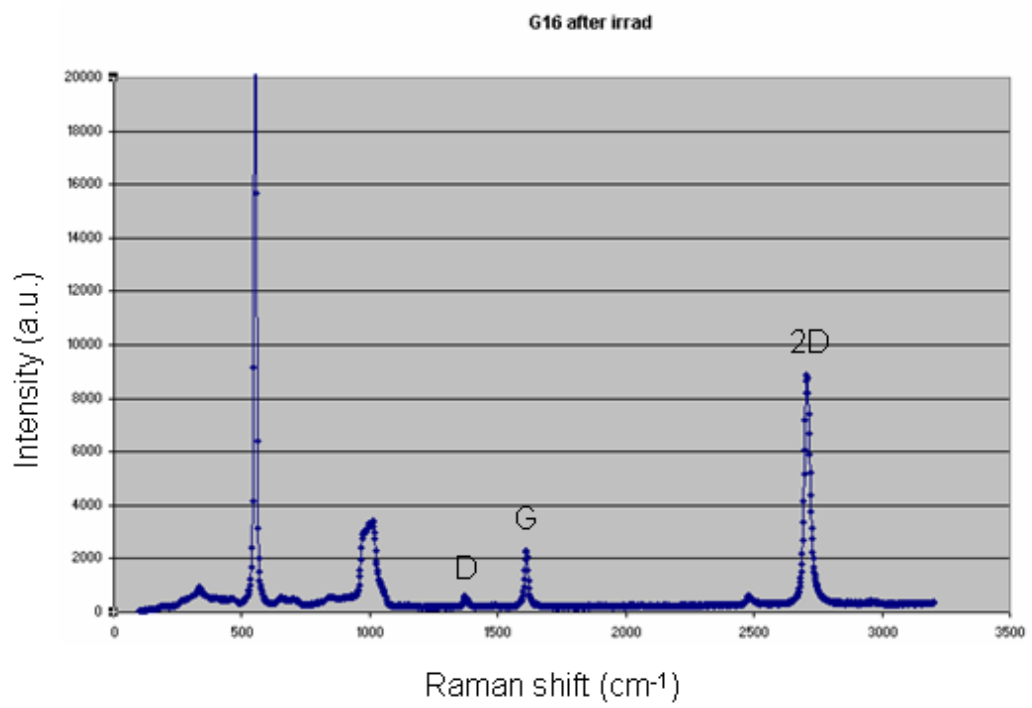

Fig. 6.4 Raman spectrum of the graphene flake plotted in fig. 6.4, after irradiation.

A comparison between the two spectra suggests a modest structural change: the D peak of the spectrum belonging to the after-irradiation sample is more pronounced, arising well above the noise level of the background. With respect to the spectrum of the sample before irradiation, the ratio between the 2D and G peak has increased. Also, a frequency shift has occurred for all the peaks. These two effects, however, appear in the Raman spectra of all the flakes that have been compared before and after irradiation.
It should be mentioned, though, that in the case of irradiation by ion accelerator, Raman results obtained in this work are not always consistent and cannot be used to draw any absolute conclusion.

Different is the situation of samples irradiated by FIB. Fig. 6.5 and 6.6 plot Raman spectra of a contacted graphene flake before and after irradiation by FIB.

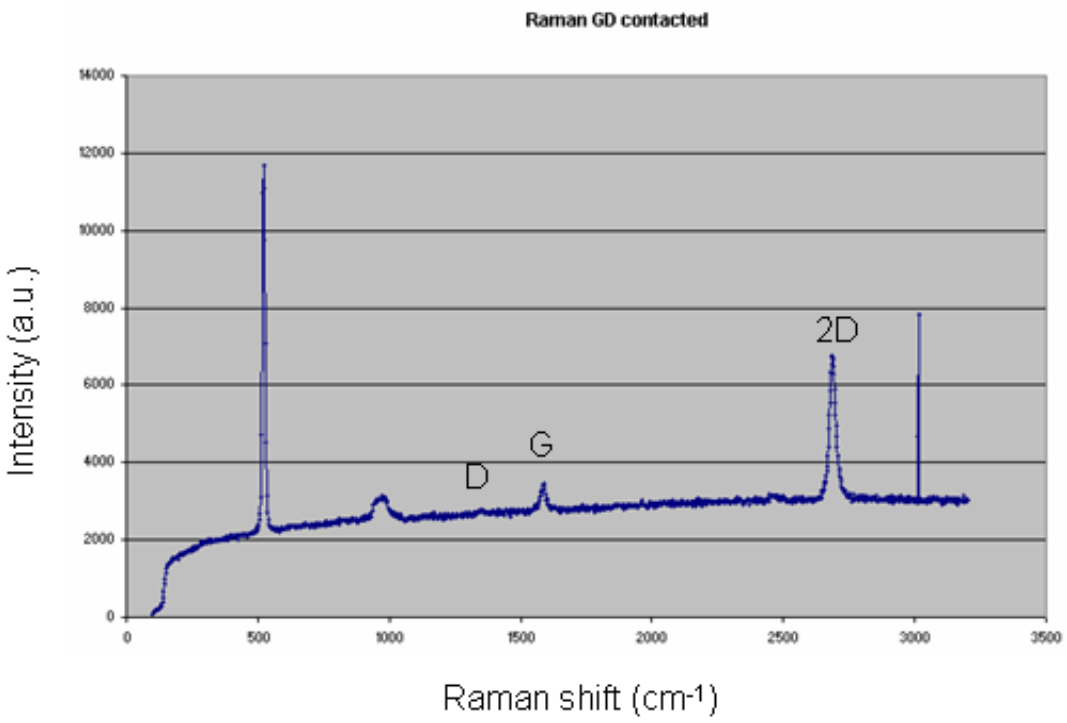

Fig. 6.5 Raman spectrum of a contacted graphene flake on SiO_2, before irradiation.

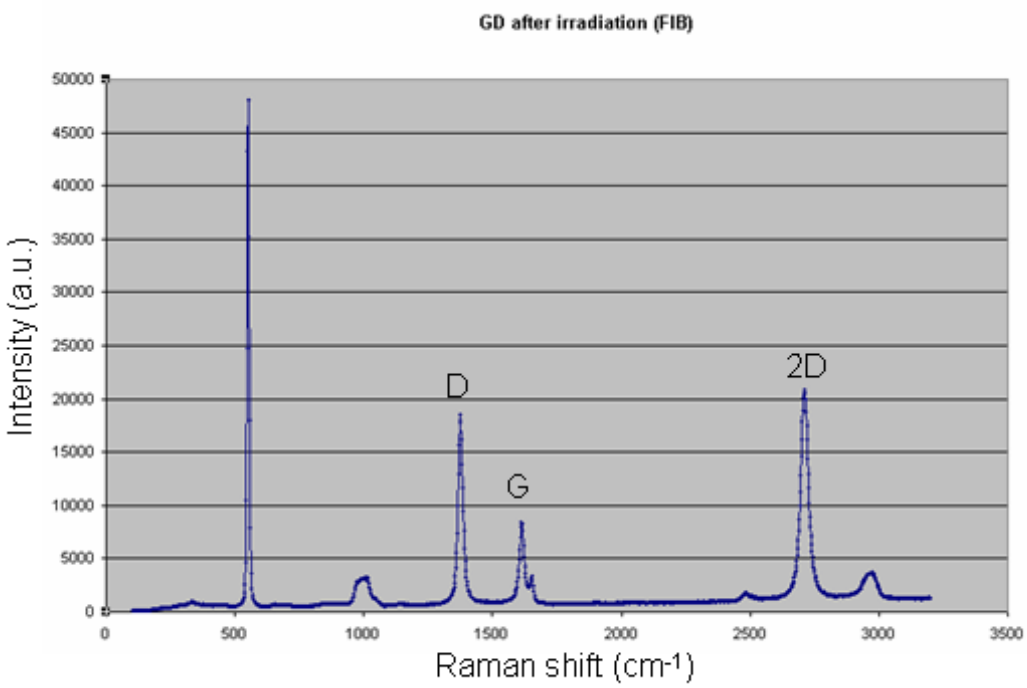

Fig. 6.6 Raman spectrum of the graphene flake plotted in fig. 6.5, after irradiation.

In this case, we can notice a relative big change in the intensity of the D peak, which indicates that a big amount of defects have been induced in the graphene flake during irradiation.

Similarly to the all other contacted samples analyzed in this work, a significant background signal appears in the spectrum before irradiation. As discussed in paragraph 4.2.3, this continuous background might be due to the gold grains in the EBL contacts that enhance the Raman signal of a fluorescence effect. The spectrum of the sample after irradiation shows a much lower background. We don't know the origin of this behaviour, but it might be due to the fact that during irradiation the sample has been partially cleaned by the heat created.

6.3 *In-situ* electrical characterization

I-V curves can measure in a quantitative way the change in electrical properties induced by the irradiation and the formation of defects.

The results of the first experiment was completely unexpected and could not be directly correlated to the properties of graphene. They have however provided some important information that helped us optimizing the setup and experimental parameters for the subsequent irradiation experiments at the Tandem.

In connection with the irradiation, the vacuum quality degraded beyond the safe operational level and a significant increase in the sample temperature was detected once the sample was quickly dismounted. These observations indicate that the power transferred from the ion beam to the sample-contacts-chipholder assembly was much higher than the heat drain through the holder into the surroundings, leading to a rapid increase in the temperature of sample assembly estimated to be of the order of 200 °C or more.

It is not yet clear how the sudden increase in current is related to the heating. It could be due to different factors: the semimetallic nature of graphene dictates that an increase in temperature leads to a decrease in resistivity; the higher temperature has induced outgassing (as confirmed by the deterioration of the vacuum level) and ionized gases might have created alternative conductive paths between the contacts, either directly or by contaminating the sample; charges implanted in the substrate just under the graphene flake might have induced a local field that altered the resistivity.

To try to avoid or at least reduce these effects, a shielded mounting was developed (Fig. 5.5) to limit the ion irradiation to a small area on the chipholder. However, this would mean that the shield itself might become very hot, therefore it was decide to minimize the power transfer during experiments with contacted flakes by using light ions at low energy (2 MeV H^+). For non-contacted flakes the heating effect is less problematic, as they are mounted directly on a metallic plate (a better heat sink) and there are not as many components that could outgas.

After several solutions were implemented (such as an accurate choice of the kind and the energy of the incident ion and the presence of the metallic shield on top of the cheapholder) a more satisfactory result was obtained. Fig. 6.7 plots the current measured on the flake with respect to the time (*i.e.* to respect to irradiation) during the first part of the second experiment carried out by the Tandem accelerator.

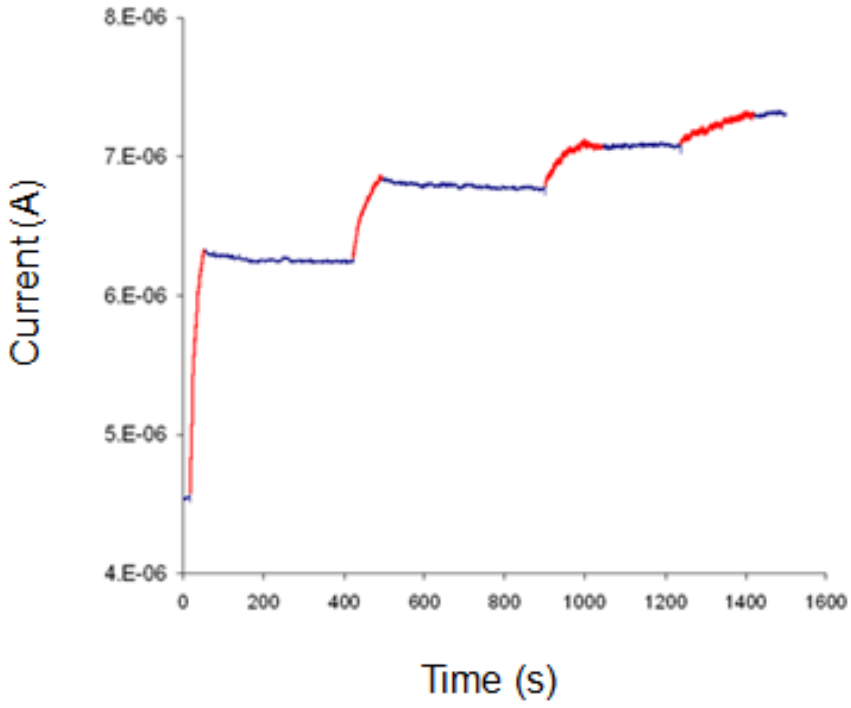

Fig. 6.7 In-situ electrical measurements. The red line marks the time when the ion beam was on (irradiation). In correspondence of the blue line the ion beam was off.

We can clearly see from the graph that the conductivity prominently increases during irradiation as expected from previous works and theoretical calculations. As soon as the ion beam is switched off, the conductivity stays more or less constant.

Fig. 6.8 reports the trend of the conductivity measured during the all duration of the experiment.

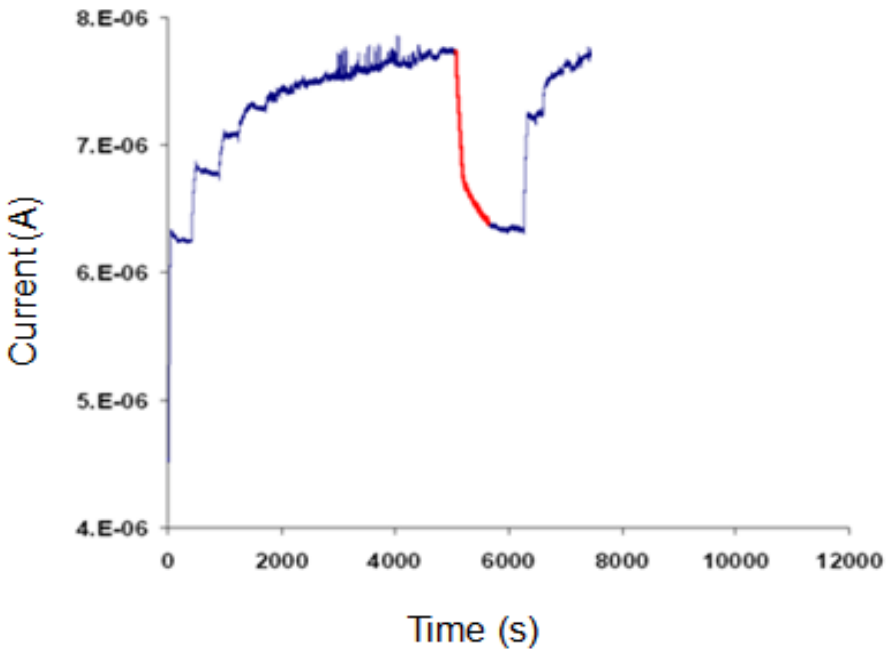

Fig. 6.8 In-situ electrical measurements taken during the duration of the all irradiation. The red line marks the moment when the vacuum in the chamber have been broken.

At some points of the experiment, the vacuum in the chamber was deliberately broken. We can notice that the conductivity immediately decreases. After the chamber was pumped down again, the conductivity though does not change until a new irradiation is performed.

Different results were obtained during FIB irradiation. Fig. 6.9 and 6.10 show the resistivity change with respect to the time during two irradiation slots performed by FIB. The red spots on the graph indicate when the sample was exposed to the ion beam.

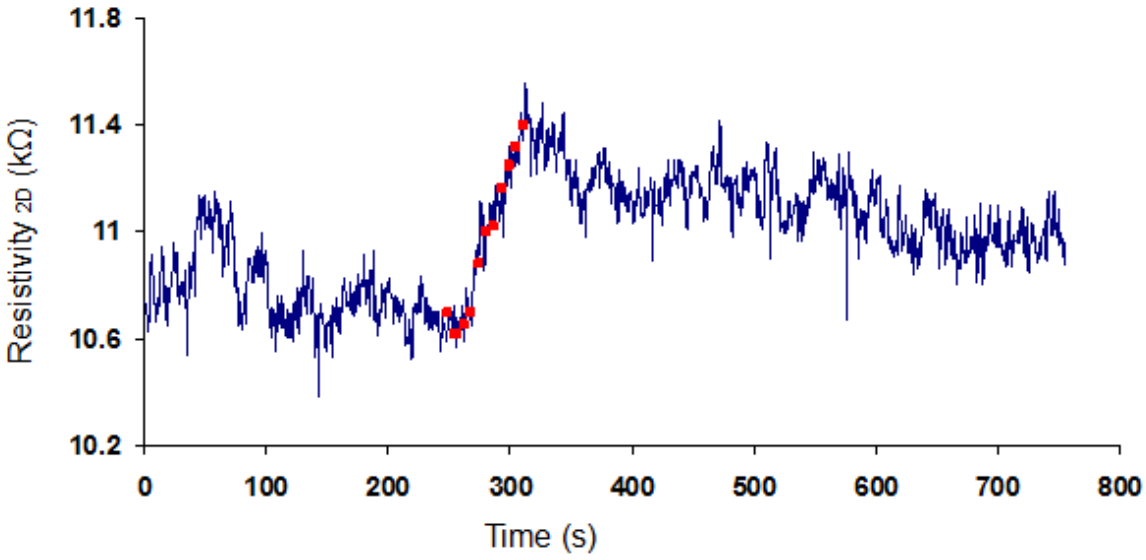

Fig. 6.9 In-situ electrical measurements taken during FIB irradiation (part I). The red spots indicates when the sample has been exposed to the ion beam. marks the moment when the vacuum in the chamber have been broken.

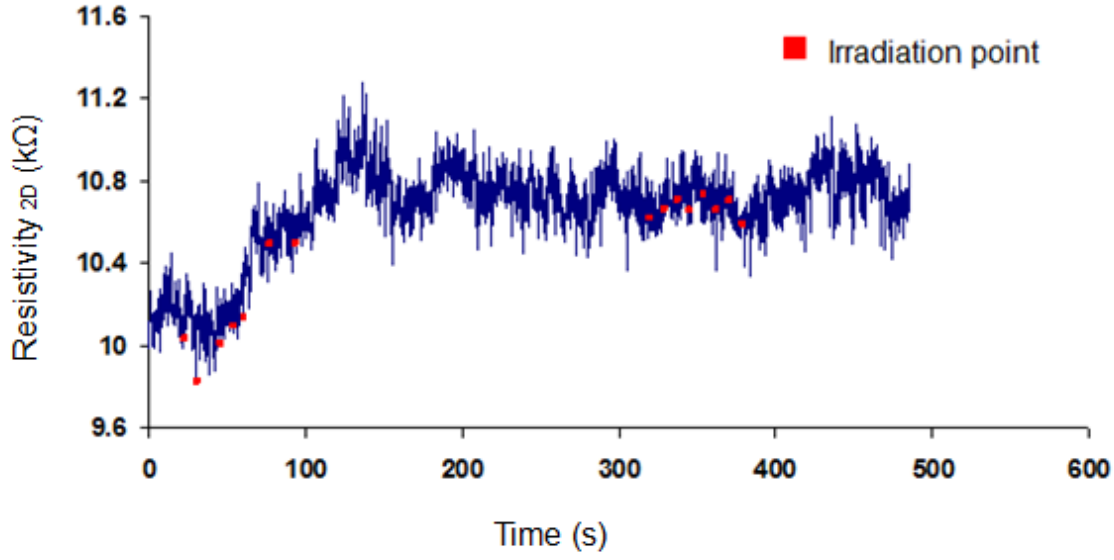

Fig. 6.10 In-situ electrical measurements taken during FIB irradiation (part II). The red spots indicates when the sample has been exposed to the ion beam. marks the moment when the vacuum in the chamber have been broken.

Differently from the case of the Tandem ion accelerator, FIB irradiation causes an increase of the resistivity. A first ion irradiation, occurred at least 100 µm away from the flake with a scan time of 80 ms, was performed on the flake by mistake. The next irradiation was performed with a scan time of 8 ms for 8 scans. The total scan time was 64 ms. This irradiation did not show any change in the resistivity, and for this reason, another irradiation with a 10 times increased scan time (80 ms) was performed. A sharp increase of the resistivity can be seen as effect of irradiation.

The I-V behavior shown during FIB irradiation is the opposite of the one shown during proton irradiation. This seems to agree with the theoretical prediction (Fig. 3.1) of an initial increase of conductivity for low defect densities (inducing additional states at the Fermi level), followed by a decrease of conductivity for higher defect densities (increase in the scattering center once the Fermi level has been saturated by gap states). This strongly suggests, together with the variations in the Raman spectra, that the doses used during the irradiation with protons induce a defect concentration <0.5%, corresponding to the first region of the curve in figure 3.1; whereas during the irradiation by FIB, a larger amount of defects were induced, corresponding to the second part of the curve (defect concentration > 0.5%).

7. Conclusions and future perspectives

Before entering into the merit of the work done so far, it should be said that the experiments performed in this work are only the initial steps of a much broader research project. The present work could be regarded as a benchmark test to assess the feasibility of the experimental setup itself and to figure out the optimum settings for the experimental parameters involved.

The most important conclusion, at this stage of the experiment, is that we have been able to build up a working setup capable of measuring the I-V response *in situ* both in the FIB and in the ion accelerator at the Tandem lab. However, the optimization of all the experimental parameters is still needed in order to achieve control over the induction of defect.

AFM and Raman spectroscopy, although useful tools for the study of graphene, cannot provide any quantitative information about the structural and electronic change induced by the irradiation and the formation of defects. I-V curves, on the contrary, can provide quantitative measurements of electrical properties change induced by irradiation.
Furthermore, conductivity measurements taken during the irradiations have revealed that by using the FIB rather than the ion accelerator at Tandem laboratory, seems to be possible to explore the two different regimes of the theoretical curve presented in Fig. 3.1. This means that the amount of defects induced by the FIB is too high, even at the beginning of the irradiation, to obtain the initial increase of the conductivity. On the other hand, the Tandem accelerator could be used to achieve both regimes by simply increasing the dose by increasing the exposure time, possibly with a series of short exposures separated in time to allow for dissipation of excess heat. The possibility to operate on the two branches of the curve in fig. 3.1 could be in principle exploited to design electronic circuit on graphene. The high resistivity part of the circuit could be

patterned on the graphene sheet by the high precision ion beam of the FIB; the entire flake is then exposed to the Tandem ion beam to increase the conductivity on the rest of the flake, as this slight increase in defect density will have a negligible effect on the regions previously exposed to the FIB.

An important factor that should be taken into account in future experiments is the interaction with the underlying substrate, which can affect the properties and the structure of the graphene layer. To avoid this unwanted effect, a good way to approach the experiment is to work with suspended graphene. Even though the difficulties regarding production and characterization are not trivial, the use of suspended graphene would eliminate the problems of substrate interactions.

8. References

[1] K. Kim et al. “Electric properties evolution of structurally defected multilayer graphene” Nano Letters 8 (10) 3092-3096 (2008).

[2] Chen. J. et al. “Defect scattering in graphene” Phys. Rev. Lett. 102, 236805 (2009).

[3] Tapaszto. L. et al. “Tuning the electronic structure of graphene by ion irradiation” Physical review B 78, 233407 (2008).

[4] A.K. Geim, K.S. Novoselos. “The rise of graphene” Nature Materials 6 (3): 183-19 (2007).

[5] Peierls , et al. Ann. I. H. Poincare 5, 177-222 (1935) - Landau, L. D. et al. Phys. Z. Sowjtunion 11, 26-35 (1937).

[6] Meyer *et al*. “The structure of suspended graphene sheets” Nature 446, 60-63 (2007).

[7] M.I. Katsnelson, K.S. Novoselov.. “Graphene: New bridge between condensed matter physics and quantum electrodynamics.” Solid state communication 143: 3-13 (2007).

[8] Castro Neto A. Et al. “The electronic properties of graphene” Reviews of modern physics 81(1): 109-162 (2009).

[9] Blake P. et al. “making graphene visible” Applied physics letters 91, 063124 (2007).

[10] Arantxa V. et al. “Principles of atomic force microscopy (AFM)” Physics of advanced material school winter 2008.

[11] M. Calleja, M. Tello, et al. “size determination of field-induced water menisci in monocontact atomic force microscopy.” Journal of Applied physics 92 (9): 5539-5542 (2002).

[12] F. Cavalca. “Master thesis”. Politecnico di Milano, Italy. (a.a 2008-2009).

[13] Ferrari. A. C. et al. “Raman spectrum of graphene and graphene layers” Physical review letters 97, 187401 820069.

[14] “Raman spectroscopy basis” Princeton Instruments.

[15] Widenkvist E. “PhD thesis: Fabrication and Functionalization of graphene and other carbon nanomaterials in solution” Uppsala Univeristy. 2010.

[16] A.C. Ferrari, J.C.Meyer, et al. “Raman Spectrum of Graphene and Graphene Layers.” Physical Review Letters 97 (18): 187401-4 (2006).

[17] T. Blom “PhD thesis: Fabrication and Application of a focused Ion Beam Nanocontact Platform for Electrical Characterization of Molecules and Particles” Uppsala university. 2010.
[18] Jafri H. et al. “Conductivity engineering of graphene by defect formation” Journal of Physics, 43, 045404 (2010).
[19] Dresselhaus et al. Phys Rev B 1981; 24: 1027-91.
[20] Compagnini G. et al. “Ion irradiation and defect formation in single layer graphene” Elsevier 47: 3201-3207 (2009).
[21] N. Buraglio, “PhD thesis: Accelerator mass spectrometry of ^{129}I and its applications in natural water system” Uppsala University. 2000.
[22] J. P. Biersack and L. Haggmark, Nucl. Instr. and Meth., vol. 174, 257, 1980.